On the dynamics of ultra-relativistic electrons (>2 MeV) near L* = 3.5 during 8 June 2015

Benjamin Hogan[1], Xinlin Li[2], Zheng Xiang[3], Hong Zhao[4], Yang Mei[5], Declan O'brien[6], Daniel N. Baker[5], and Shrikanth G. Kanekal[7]

[1]CU Boulder
[2]Laboratory for Atmospherics and Space Physics (LASP)
[3]Wuhan University
[4]Auburn University
[5]University of Colorado Boulder
[6]University of Colorado, Boulder
[7]NASA/Goddard Space Flight Center, Greenbelt, Maryland, USA

August 4, 2023

Abstract

Understanding local loss processes in Earth's radiation belts is critical to understanding their overall structure. Electromagnetic ion cyclotron waves can cause rapid loss of multi-MeV electrons in the radiation belts and contribute to an uncommon three-belt structure in the radiation belts. These loss effects have been observed at a range of L* values, recently as low as L* = 3.5. Here, we present a case study of an event where a local minimum develops in multi-MeV electron phase space density near L* = 3.5 and evaluate the possibility of EMIC waves in contributing to the observed loss feature. Signatures of EMIC waves are shown including rapid local loss and pitch angle bite outs. Analysis of the wave power spectral density during event shows EMIC wave occurrence at higher L* values. Using these representative wave parameters, we calculate minimum resonant energies, diffusion coefficients, and simulate the evolution of electron PSD during this event. From these results, we find that O+ band EMIC waves could be contributing to the local loss feature during this event. O+ band EMIC waves are uncommon, but do occur in these L* ranges, and therefore may be a significant driver of radiation belt dynamics under certain preconditioning of the radiation belts.

On the dynamics of ultra-relativistic electrons (>2 MeV) near L* = 3.5 during 8 June 2015

Authors: Benjamin Hogan[1,2], Xinlin Li[1,2], Zheng Xiang[3], Hong Zhao[4], Yang Mei[1,2], Declan O'Brien[1,2], Daniel N. Baker[1,2], Shrikanth Kanekal[5]

[1]Laboratory for Atmospheric and Space Physics, University of Colorado Boulder, Boulder, CO, USA. [2]Department of Aerospace Engineering Sciences, University of Colorado Boulder, Boulder, CO, USA. [3]Department of Space Physics, School of Electronic Information, Wuhan University, Wuhan, China. [4]Department of Physics, Auburn University, Auburn, AL, USA. [5]NASA Goddard Space Flight Center, Greenbelt, MD, USA.

Corresponding author: Benjamin Hogan (ben.hogan@lasp.colorado.edu)

Key points

1. A local minimum in >2 MeV electron phase space density is shown to form rapidly near L*=3.5 during a moderate storm of minimum Dst=-67 nT
2. EMIC wave characteristics are shown during this event, and we use quasi-linear theory to evaluate their role in this loss
3. Pitch-angle diffusion simulations with scattering rates due to O+ band EMIC waves are shown to reproduce the observed loss at L*=3.5

Abstract

Understanding local loss processes in Earth's radiation belts is critical to understanding their overall structure. Electromagnetic ion cyclotron waves can cause rapid loss of multi-MeV electrons in the radiation belts and contribute to an uncommon three-belt structure in the radiation belts. These loss effects have been observed at a range of L* values, recently as low as L* = 3.5. Here, we present a case study of an event where a local minimum develops in multi-MeV electron phase space density near L* = 3.5 and evaluate the possibility of EMIC waves in contributing to the observed loss feature. Signatures of EMIC waves are shown including rapid local loss and pitch angle bite outs. Analysis of the wave power spectral density during event shows EMIC wave occurrence at higher L* values. Using these representative wave parameters, we calculate minimum resonant energies, diffusion coefficients, and simulate the evolution of electron PSD during this event. From these results, we find that O+ band EMIC waves could be contributing to the local loss feature during this event. O+ band EMIC waves are uncommon, but do occur in these L* ranges, and therefore may be a significant driver of radiation belt dynamics under certain preconditioning of the radiation belts.

1. Introduction

Earth's radiation belts are normally a two-belt structure of energetic particles, with an inner belt which consists primarily of 100s of keV electrons and 10s to 100s of MeV protons with peak fluxes at L ≈ 2-3, and an outer belt of mainly 100s of keV to >MeV electrons with peak intensity near L = 4-5. L is the McIlwain L value, the distance in Earth radii (R_E) at which a dipole field line crosses the geomagnetic equatorial plane (McIlwain, 1961). The high energy electron populations in the outer belt exhibit various dynamics due to solar driving of the magnetosphere. The Van Allen Probes (formerly known as Radiation Belt Storm Probes, or RBSP) mission has provided valuable insight to the behavior of these energetic particles (Mauk et a., 2012). One of the early discoveries of the Van Allen Probes era was the identification of a third radiation belt, a storage ring of multi-MeV electrons near the inner edge of the outer radiation belt which is not generally observed (Baker et al., 2013). This was characterized by a reduction in flux of multi-MeV electrons in the region 3.5 < L* < 4.0 resulting in local peaks in fluxes in the region 3.0 < L* < 3.5 and at L* > 4.0. L* is the Roederer L value and is inversely proportional to the third adiabatic invariant (Roederer 1970), and L* ≈ L for the low values of interest discussed here, although their unit is different (Roederer and Lejosne, 2018, Xiang et al., 2017).

Various driving mechanisms in the inner magnetosphere cause dynamics of trapped particle populations. Here, we highlight effects most prevalent in the dynamics of these multi-MeV electrons in the radiation belts. Phase space density (PSD) is often used to visualize these mechanisms, which is related to particle flux divided by the square of the particle's momentum (e.g., Chen et al., 2006). Trapped particles will undergo radial diffusion, a process referred to as a random walk due to varying electric and magnetic fields around the Earth (e.g., Barker et al., 2005; Lesjone et al., 2020). Radial diffusion will cause particles to reduce local radial gradients that develop in PSD (e.g., Green & Kivelson, 2004). The Dst effect changes the drift orbit radius of trapped particles during geomagnetic storms, as drift shells increase in radius to conserve the third adiabatic invariant in response to the reduction in Earth's magnetic field strength, resulting in a measured reduction in flux at a fixed radial distance as particles move outward (Kim & Chan et al., 1997; Li et al., 1997). This process is an adiabatic process and PSD will reverse to pre-storm levels with the recovery of Dst. Magnetopause shadowing is another driver of dynamics which occurs during storms when the solar wind compresses Earth's magnetosphere inward and reduces the last closed drift shell (LCDS) (e.g., Turner et al., 2014, Xiang et al., 2018). Particles outside of the LCDS are lost and particles near the LCDS are then exposed to rapidly formed gradients in PSD due to the outward loss of particles. Earthward particles of the LCDS then radially diffuse outward toward the gradient near the magnetopause and can also be lost outward of Earth's magnetosphere.

Wave-particle interactions can also cause loss of radiation belt populations and are energy-dependent due to resonance conditions with the timescales of invariant motions of trapped particles. Chorus waves can cause precipitation of MeV electrons on timescales of several days (Orlova & Shprits, 2014). Chorus wave loss is generally observed outside of the plasmasphere, a region of dense cold plasma with a varying outer boundary generally confined to L<4 (e.g., Thorne 2010). Hiss waves are observed within the plasmasphere and can preferentially scatter several hundreds of keV electrons (e.g., Ni et al., 2019; Zhao et al., 2019). Hiss waves can also cause weak loss of MeV electrons on timescales of days to months (Malaspina et al., 2016; Selesnick et al., 2003; Thorne et al., 2013). Another type of wave which prominently affects MeV energy electrons are electromagnetic ion cyclotron (EMIC) waves (e.g., Summers et al., 2007). EMIC waves effects are observed as fast, local losses of multi-MeV electrons satisfying resonance conditions (e.g., Aseev et al., 2017; Drozdov et al., 2019, 2020, 2022; Shprits et al., 2016, 2017; Usanova et al., 2014; Xiang et al., 2017). Local extrema which form due to these loss processes can result in radiation belt features such as the third radiation belt. The three-belt structure first reported by Baker et al., (2013), with a storage ring of multi-MeV electrons found near the inner edge of the outer belt, is shown to be reproduced in simulation models only with the inclusion of EMIC wave effects (Shprits et al., 2016). Therefore, understanding the effects of EMIC waves on multi-MeV electron populations near the inner edge of the outer belt is critical to understanding the overall structure of the radiation belts. Their effects on multi-MeV electrons are characterized in recent studies using the rich data collected by the Van Allen Probes Relativistic Electron Proton Telescope (REPT) data, with notable features such as multi-MeV electron loss by up to 2 orders of magnitude within satellite passes, limiting electron lifetimes, and producing bite outs in the pitch angle spectra (Baker et al., 2021; Su et al., 2017). We present here a discussion of the EMIC wave loss mechanism.

EMIC waves pitch angle scatter electrons into the loss cone via doppler-shifted resonance with electrons (Thorne and Kennel, 1971). EMIC waves most easily scatter particles at low equatorial pitch angles already near the loss cone, and narrowing of the pitch angle spectra, or "bite-out" features in multi-MeV electron flux have been shown to accompany EMIC wave occurrences (e.g., Aseev et al., 2017; Usanova et al., 2014). However, these studies have not made efforts to numerically quantify the relationship between flux evolution due to EMIC waves and the development of these bite outs. To decrease the entire pitch angle spectra, other waves that have stronger effects at all pitch angles such as chorus and hiss waves are likely required in concert with EMIC waves to produce whole-spectra losses (Drozdov et al., 2020; Ross et al., 2021). EMIC waves can only affect electrons of above specific energies, described as the minimum resonant energy of the electrons (e.g., Summers & Thorne, 2003). The minimum resonant energy as a function of pitch angle is dependent upon the solution of the plasma dispersion relation describing the wave behavior in the local plasma environment. Local loss processes such as EMIC wave scattering are apparent in radial PSD profiles as rapid decay at a specific L* value where the EMIC waves are present which can induce local minimums.

However, variations in L* locations of EMIC wave effects on multi-MeV electrons are reported; for example, at L* = 4.0 (Shprits et al., 2017, 2022), at L* = 4.2 (Lyu et al., 2022), L*> 4.2, (Xiang et al., 2017), L* = 4.5 (Usanova et al., 2014), and at L* = 4.7 (Aseev et al., 2017) during various events. A study of Van Allen Probes and GOES observations by Drozdov et al., (2022) showed that local PSD minimums are most common for several-MeV electron populations in the range L* = 4-5. Furthermore, the PSD minimums reported by the study by Drozdov et al., (2022) were reproduced only with EMIC wave effects included in a simulation model. A study by Cervantes et al., (2020) of Van Allen Probes data from October 2012-2016 found that EMIC waves on average affect $\mu \geq 900$ MeV/G electrons in the range L* = 3.6 - 6 and are the dominant loss process during storms near the inward edge of multi-MeV electron loss observations. Clearly, variations exist in the spatial extent of EMIC wave induced PSD minimums of multi-MeV electrons. Furthermore, the inward location of these PSD features and their driving mechanisms must be understood due to their contributions of local minimums in multi-MeV electron populations which contributes to the formation of the three-radiation belt structure. Hogan et al., (2021) reported an energy-dependent local minimum in multi-MeV electron PSD that forms over a long-term period from March to June 2015 near L* = 3.5, lower than where EMIC wave-induced loss has been reported before with event studies. PSD minimums in this L* region can be difficult to find with automatic detection algorithms such as those used by Drozdov et al., (2022) due to low PSD at small L* values. The dwell time of the spacecraft also decreases at low L* value, making the occurrence of these features less likely to be reported (e.g., Chen et al., 2019, Saikin et al., 2015, Sigsbee et al., 2023).

Statistical studies of EMIC wave occurrence during the Van Allen Probes era describe the spatial occurrence and frequency of these waves. Saikin et al., (2015) compiled EMIC wave observations using Van Allen Probes data from 2012-2015 and Sigsbee et al., (2023) studied the same data set until June 2016. Both studies showed that most observations of H+ and He+ band EMIC waves occur between L = 4-6, and O+ band waves are mostly observed at L < 2-4. Chen et al., (2019) studied the Van Allen Probes data set until 31 December 2017 and reported H+, He+, and O+ band EMIC waves to occur primarily in the regions $5 \leq L \leq 6.5$, $3 \leq L \leq 4.5$, and $3 \leq L \leq 4$ for each species. The majority of EMIC events, regardless of wave band, occur in the region $5 \leq L \leq 6$, with 35% of EMIC waves observed are in the H+ band, 59% were He+ band, and 7% were O+ band waves (Saikin et al., 2015). Sigsbee et al., (2023) report EMIC waves are observed ~2.4% of the time during the Van Allen Probes era, considering data from both Probes. Studies by Yu et al., (2015) suggest that O+ band waves can grow strongly near the plasmapause boundary region where the oxygen torus forms (e.g., Nosé et al., 2015), thus their increased observational occurrence in the low L region.

This study analyzes a moderate storm on 8 June 2015 during which Hogan et al., (2021) reported the formation of a local minimum in PSD in March-June 2015 at $L^* = 3.5$, lower than where EMIC wave-induced local minimums had been reported before and lower than where the more common H+ and He+ EMIC waves are generally observed. We investigate the physical mechanism responsible for this local minimum by analysis of multi-MeV electron measurements, wave observations by the spacecraft, and consideration of wave particle interaction theory for the local plasma environment. PSD and flux features shown during the event are consistent with prior observations and theory of multi-MeV electron interactions with EMIC waves. EMIC waves in the O+ band will be shown to be the most likely contributor of this minimum from analysis using wave-particle interaction theory. Analysis of the wave power spectral density during the event is conducted and calculation of minimum resonant energies and diffusion coefficients for representative EMIC waves during the event are found. These diffusion coefficients are then used in a one-dimensional pitch-angle diffusion simulation to model the effects of EMIC waves during the event of study, showing the feasibility of O+ band EMIC waves in contributing to the observed loss. We discuss these results and present conclusions for the reader.

2. Instrumentation and methods

2.1. Data

Data from the Van Allen Probes mission is utilized for this study (Mauk et al., 2012). The Van Allen Probes consisted of two nearly identical probes launched into near-identical following orbits on 30 August 2012 and provided near-continuous measurements of the radiation belts until 18 October 2019 (Probe A) and 19 July 2019 (Probe B). Various onboard instruments provided simultaneous measurements of particles and waves in the radiation belts. The Energetic Particle Composition and Thermal Plasma Suite (ECT) provided energetic particle measurements and included the Relativistic Electron Proton Telescope (REPT) instrument (Baker et al., 2012). REPT provides >MeV electron energy measurements with high count rates, even at low L values where fluxes are low, due to its large geometric factor (0.2 cm^2sr). We use this electron flux data to calculate electron PSD (e.g., Chen et al., 2006). The ECT Magnetic Ephemeris files (MagEphem) are also utilized here, in which adiabatic coordinates have been computed for selected magnetic field model configurations. Here, we use calculated adiabatic coordinates found using the TS04D magnetic field model, which should account for storm-time differences in the magnetic field (Tsyganenko & Sitnov, 2005). Magnetometer data from the Electric and Magnetic Field Instrument Suite and Integrated Science (EMFISIS) (Kleitzing et al., 2013) is inspected using methods for analyzing a tri-axial magnetometer (Bortnick et al., 2009; Usanova et al., 2012). We also use data from EMFISIS for obtaining an estimate of the local number density of electrons from analysis of the observed upper-hybrid frequency, identification of the plasmapause boundary, and determining the local magnetic field strength.

2.2. Theory

Wave-particle interaction theory predicts the energy exchange behavior of a wave and a trapped particle's invariant motion. L-mode EMIC waves are expected to have doppler-shifted gyroresonance with electrons of given energies (Kennel and Thorne, 1971). This is true when the following resonance condition is satisfied:

$$\omega - kv_{||} = N|\Omega_e|/\gamma \tag{1}$$

where ω is the frequency of the wave, k is the parallel wave number found from the plasma dispersion relation, N is the cyclotron resonance harmonic, Ω_e is the electron gyrofrequency, $\gamma = (1 - v^2/c^2)^{-1/2}$ is the Lorentz factor, $v = (v_{||}^2 + v_{\perp}^2)^{1/2}$ is the electron speed, and $v_{||}$ and $v_{\perp}$ are the velocity components parallel and perpendicular to the ambient magnetic field. The minimum energy of electrons E_{min} (in units of $m_e c^2$) that will have gyrofrequencies which satisfy resonance this resonance condition is:

$$E_{min} = \left[1 - (v_{||})^2/c^2\right]^{-1/2} - 1 \tag{2}$$

where $v_{||}/c$ is the ratio of the particle's parallel velocity $v_{||}$ to the speed of light c, and $v_{||}$ is found via the solution of equation (1) which therefore depends on the solution of a plasma dispersion relation (e.g., Summers & Thorne 2003). Here, we assume a cold plasma dispersion relation as described by Summers & Thorne (2003) and Summers et al., (2007). The strength of pitch angle scattering by L-mode EMIC waves can also be quantified by quasi-linear interaction theory as described by the pitch angle diffusion coefficient $D_{\alpha\alpha}$. $D_{\alpha\alpha}$ as described by Summers et al., (2007) for these waves is:

$$D_{\alpha\alpha} = \frac{\pi}{2}\frac{1}{\rho}\Omega_e^2\frac{1}{(E+1)^2}\sum_j \frac{R(1-\frac{x_j cos\alpha}{y_j \beta})^2|dx_j/dy_j|}{\delta x|\beta cos\alpha - dx_j/dy_j|}e^{-(\frac{x_j - x_m}{\delta x})^2} \quad (3)$$

where ρ describes the Gaussian spectral density of the wave, Ω_e is the electron gyrofrequency, E is the dimensionless particle kinetic energy, $\beta = [E(E+2)]^{1/2}/(E+1)$, R is the ratio of the relative wave power, x_j and y_j are the wave frequencies and wave numbers which are the resonant roots for the wave found from the plasma dispersion relation, δx and x_m are also found from these roots, and j is the number of roots. See Summers et al., (2007) for a full discussion of this equation. The solution of the minimum resonant energy of an electron with an EMIC wave (equation 2) depends on the solution of a plasma dispersion relation, which is a function of the local ion composition, number density, and magnetic field. The diffusion coefficient (equation 3) also depends on these parameters, as well as the relative power of the wave to the background magnetic field, and the assumed Gaussian spectral density of the wave power.

To compute the minimum resonant energy and diffusion coefficients for EMIC waves of interest in this study we use the Full Diffusion Code (Ni et al., 2008, 2011; Shprits and Ni et al., 2009). This model calculates minimum resonant energies and diffusion coefficients for input wave parameters based on wave-particle interaction theory described above. With the modeled diffusion coefficients, a one-dimensional pure pitch-angle diffusion equation (e.g., Ni et al., 2015) is solved numerically to simulate the time-evolution of electron phase space density:

$$\frac{\partial f}{\partial t} = \frac{1}{T(\alpha_{eq})\sin(2\alpha_{eq})}\frac{\partial}{\partial \alpha_{eq}}\left[T(\alpha_{eq})\sin(2\alpha_{eq})\langle D_{\alpha\alpha}\rangle\frac{\partial f}{\partial \alpha_{eq}}\right] \quad (4)$$

where f is phase space density, t is time, α_{eq} is equatorial pitch angle, $\langle D_{\alpha\alpha}\rangle$ is the bounce-averaged pitch angle diffusion coefficient, and the normalized electron bounce period $T(\alpha_{eq}) = 1.3802 - 0.3198[sin(\alpha_{eq}) + \sqrt{sin(\alpha_{eq})}]$ (Lenchek et al., 1961).

3. 8 June 2015 Event Study

Hogan et al., (2021) reported daily-averaged PSD between 26 March – 20 June 2015 and showed the development of a local minimum in PSD near L* = 3.5. During this period the time of greatest deepening of the observed minimum was during a moderate geomagnetic storm on 8 June 2015, where the Dst_{min} reached -67 nT. Panel a of Figure 1 shows the Dst during this event and vertical-colored lines denote times where the satellite observes multi-MeV electrons at K = 0.10

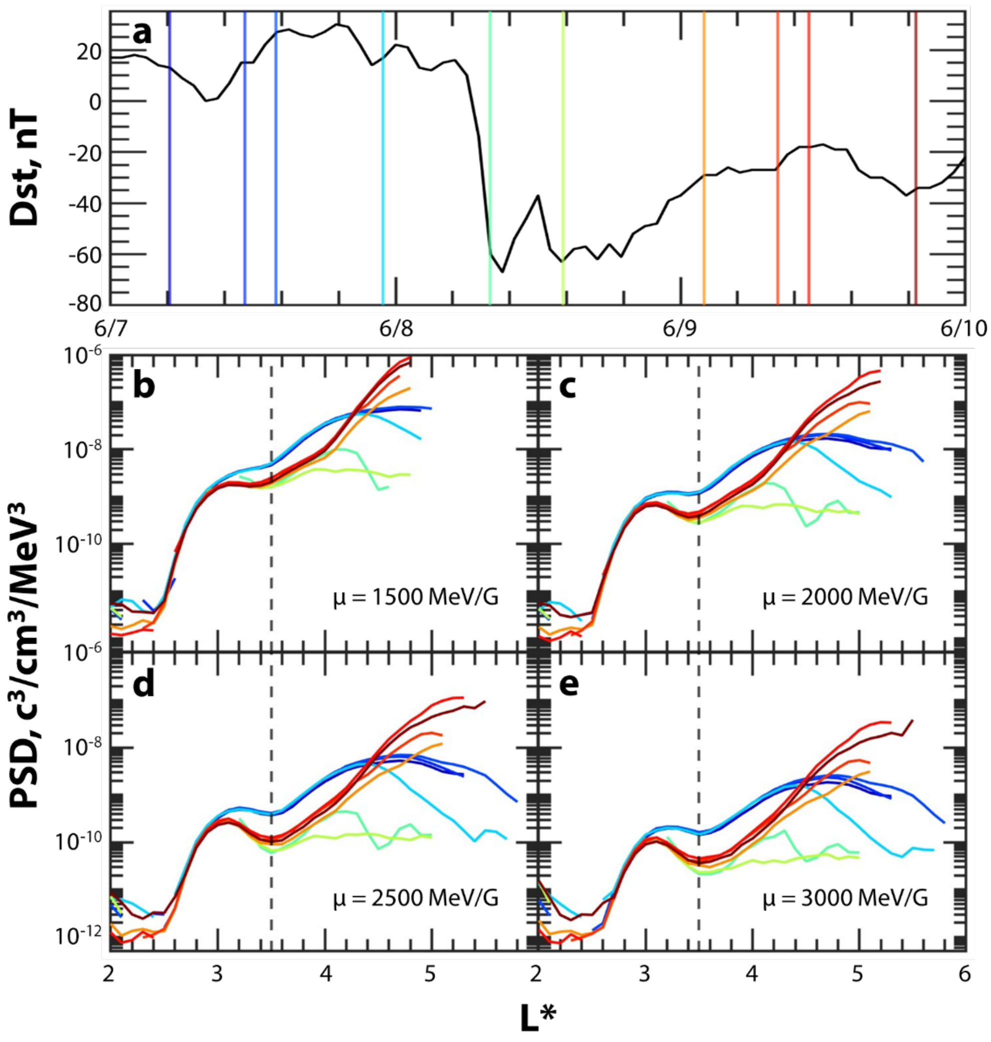

Figure 1. Panel A: Dst for 7-9 June 2015. Vertical lines indicate passes where Van Allen Probe A observes multi-MeV electrons at L* = 3.5, K = 0.10 $G^{1/2}R_E$. Panels b – e show pass averaged radial PSD profiles for K = 0.10 $G^{1/2}R_E$ and μ = 1500, 2000, 2500, and 3000 MeV/G respectively. The colors of the radial profiles correspond to the times shown for the same-colored lines in panel a. A vertical dashed line at L* = 3.5 is shown in panels b – e.

$G^{1/2}R_E$ and L* = 3.5 for 7 through 9 June 2015. These vertical lines are plotted at the center time of each of these observation bins from each satellite pass. Panels b through e show radial profiles of PSD during this period, averaged for each of these observation bins from satellite passes. The color of each profile corresponds to the passes indicated in panel a. PSD is calculated for diagnostic first adiabatic invariant values μ = 1500, 2000, 2500, and 3000 MeV/G, second adiabatic invariant value K = 0.10 $G^{1/2}R_E$, and L* bins ± 0.05. This value of K is selected as the lowest value at which multi-MeV electrons are nearly continuously observed by the Van Allen Probes mission. These narrow L* bins provide 21-28 data points per observation bin at L* = 3.5. The selected invariant values roughly correspond to 3.4, 4, 4.5, and 5.0 MeV electrons at L* = 3.5. Panel e shows that both inbound and outbound satellite passes of 3000 MeV/G electrons decrease by a factor of 6.8 within one satellite orbit near L* = 3.5 during this event, forming a local minimum in one satellite orbit. The loss is energy dependent, as seen by the increasing prominence of the minimum shown in panels B through D with increasing μ. Decreases by factors of 3.3, 4.5, 6.5, and 6.8 are shown for the 1500, 2000, 2500, 3000 MeV/G populations. Results here are shown from Van Allen Probe A. Results from Probe B for the same period are shown in the Supporting Information, and show the same local minimum at L* = 3.5 with similar decrease in one orbit, with a slight time shift due to the trailing Probe B passing the L* = 3.5 region ~one hour after Probe A. A comparison of PSD at L* = 3.5 from both spacecraft is also shown in the Supporting Information. We also note a slight variation in the precise L* location of the local minimum when found with fine L* bins 0.1 wide: at L* = 3.4, 3.5, and 3.5-3.6 for the 2000, 2500, and 3000 MeV/G electron populations. A local minimum also exists in PSD near L* = 4.5 during one satellite pass near the storm main phase, however this feature could be adiabatic as it does not exist in subsequent satellite passes, and perhaps is a function of the magnetic field model not accurately representing realistic L* values at high L* where the magnetic field can become more dynamic during the main phase of the storm.

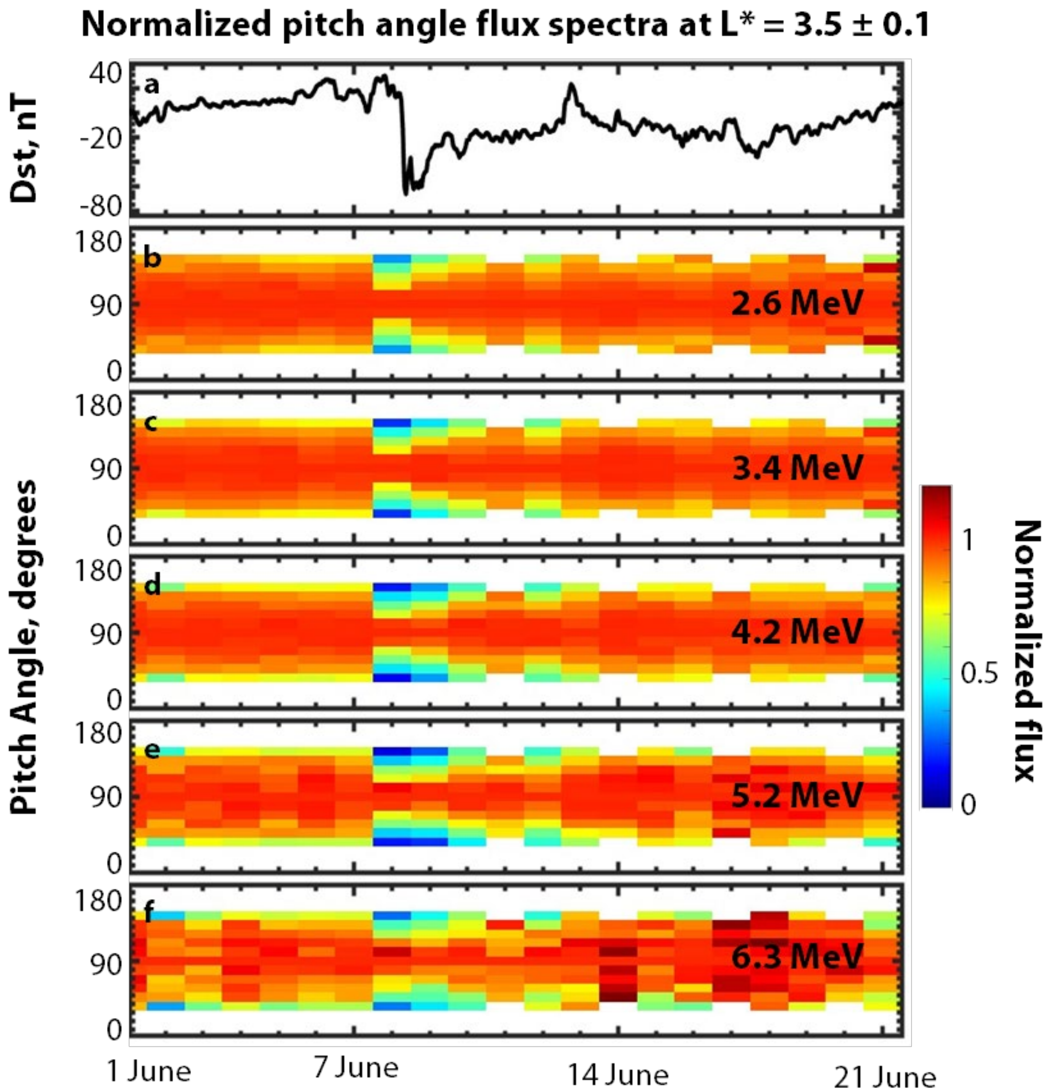

Figure 2 Dst, and daily-averaged normalized flux spectra from the 2.6 – 6.3 MeV energy channels from REPT for 1 – 21 June 2015. Data is from Van Allen Probe A. Normalized flux spectra are found by normalizing the pitch angle flux spectra to the 90-degree flux measurements.

Figure 2 shows the Dst in panel a and normalized flux spectra in panels b through f for the first three weeks of June 2015. The daily-averaged local flux spectra at L* = 3.5 are normalized in pitch angle to the 90-degree flux measurements to show the representative shape of the spectra (as in Aseev et al., 2017; Usanova et al., 2014). These measurements show that the pitch angle distribution of multi-MeV electrons is a common broad pancake distribution (e.g., Roederer 1970) in the pre-storm conditions of the event. On 8 June 2015 we show the presence of narrowing of the normalized-pitch angle spectra via strong losses in the normalized spectra at low-pitch angles relative to near-90° trapped particles, referred to as pitch angle bite outs (e.g., Bingley et al., 2019; Usanova et al., 2014). The pitch angle spectra then recover after the event to a broad pancake spectrum by 13 June for the remainder of the period shown. These bite-outs are shown in energies up to the 6.3 MeV energy channel measurements from REPT.

The wave power spectral density during 0 – 6 UT 8 June 2015 is shown in Figure 3 and is analyzed for signatures of EMIC waves. He+ and O+ gyrofrequencies are plotted and labeled in purple and are calculated using the magnitude of the measured magnetic field at the spacecraft. The H+ gyrofrequency is greater than those shown here, however, no relevant features are present in the wave power spectral density at these higher frequencies, therefore we focus on features in wave power at <5 Hz in Figure 3. We note the regions of contamination in these measurements in Figure 3. The constant power through the ion gyrofrequencies and constant vertical bands of wave power spectral density near 1:30-2:30 UT is likely instrument contamination as wave power will generally exhibit cutoffs near the gyrofrequencies due to the dampening effects of the actual ion-electron interactions (e.g., Fraser, 1985). Analysis is also conducted to find wave normal angle and ellipticity. These calculated parameters from the magnetometer data are analyzed for signatures of EMIC waves: wave power one order of magnitude greater than the average power in a frequency bin over the time range of study, wave normal angles <30 degrees, and ellipticity close to -1

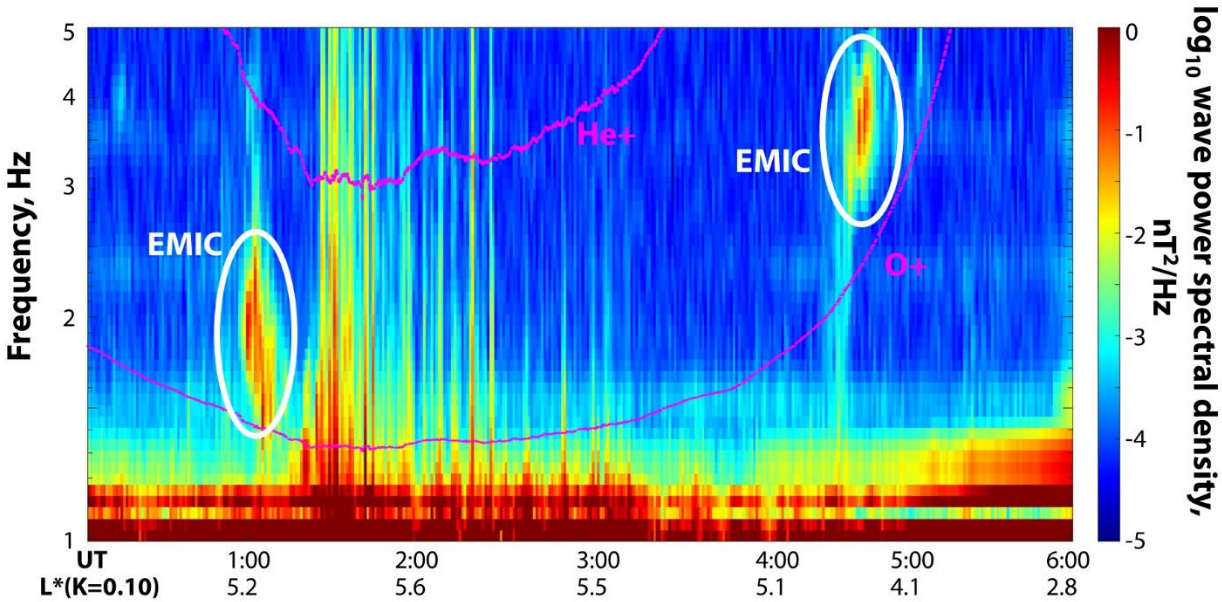

Figure 3 Wave power spectral density for 0-6 UT 8 June 2015. Data is from Van Allen Probe A. He+ and O+ ion gyrofrequencies are plotted in purple using the measured magnetic field from the EMFISIS instrument. Regions of EMIC power are identified and labeled. L* values corresponding to K = 0.10 $G^{1/2}R_E$ at each hour are reported below the x-axis.

indicating left hand polarized waves, matching EMIC wave theory and results from statistical studies of EMIC wave observations (Cao et al., 2020; Chen et al., 2019; Saikin et al., 2015). Regions in which these criteria for EMIC waves are satisfied are circled in Figure 3. Near 1:00 UT and 4:45 UT there are signatures of EMIC waves shown in the He+ band just above the O+ frequency, characteristic of where bursts of wave power are commonly observed relative to the local ion gyrofrequencies (e.g., Usanova et al., 2021). We note here this observation of EMIC waves occurs near L* = 4.2 – 4.3, higher than where the observation of rapid loss is shown near L* = 3.5. Similar analysis from RBSP B does not show any EMIC wave signatures during 7-8 June 2015.

The results in Figure 1 indicate a loss process that is energy dependent with loss which increases with μ and occurs on timescales within one 9-hour satellite orbit. The results in Figure 2 show accompanying pitch angle bite outs with these observations. The local number density is also analyzed as found from EMFISIS data and indicates local number density ~960 cm^{-3} at L* = 3.5 during the satellite pass of interest, indicating that the satellite is in a region of dense plasma and likely within the plasmapause, normally indicated by number densities >100 cm^{-3}. Local number density has also been used to identify the plasmapause crossings during the Van Allen Probes era by the EMFISIS data team. These results show that the spacecraft is within the plasmasphere during this loss event. The local number density and plasmapause crossing locations found from the local number density are shown in the Supporting Information. Plasmapause crossings of L* = 4.6 are indicated in the orbit preceding the observed loss, and compression of the plasmapause to L* = 3.9 is indicated during the pass where rapid PSD loss is first observed. Thus, the observed feature at L* = 3.5 occurs well within the plasmapause boundary. Chorus waves do not propagate well within the dense plasmapause (e.g., Meredith et al., 2001). Hiss waves can occur within the plasmapause but have not been shown to strongly affect MeV electrons on these timescales (e.g., Malaspina et al., 2016; Selesnick et al., 2003; Thorne et al., 2013). Rather, hiss waves preferentially affect 100s of keV electrons (e.g., Ni et al., 2019; Zhao et a., 2019), much lower than the >MeV populations affected here. Therefore, neither chorus nor hiss wave-particle interactions are likely to a prominent driver of multi-MeV electron dynamics during this event at L* = 3.5. PSD increases at higher L* values, suggesting no readily apparent effects of magnetopause shadowing on the trapped particle populations at L* = 3.5. The loss feature is shown to persist in pass-averaged PSD through the ~2-day period after the initial loss observation shown, and the resulting local minimum in PSD exists until a strong storm on 21-23 June 2015 in daily-averaged PSD (Hogan et al., 2021). The persistence of this feature with Dst recovery indicates that the process is not adiabatic and the Dst effect is not causing these dynamics. Furthermore, radial diffusion should oppose the formation of PSD gradients and local extrema such as reported here, thus the process occurring exceeds the effects of radial diffusion. EMIC waves are the most likely driving mechanism as their effects are strong within the plasmapause, preferentially affect electrons of increasing energies (specifically in the >MeV range), cause loss on rapid timescales, are shown to cause rapid-forming pitch angle bite outs and are shown to contribute to the formation of similar minimums in PSD at higher-L* values. EMIC waves are also observed during the satellite orbit where the rapid loss is shown, however at higher L* values. Therefore, due to the lack of likely contributions from other established drivers of multi-MeV electron loss, EMIC wave effects arise as the most likely mechanism to contribute to this PSD minimum at L* = 3.5. We here quantify the effects of EMIC waves on the PSD population observed using wave-particle interaction theory.

4. PSD simulations and comparisons with observations

We calculate minimum resonant energies and diffusion coefficients from EMIC waves using quasi-linear theory to estimate the timescale of loss due to these waves. These values are found using the full diffusion code (Ni et al., 2008, 2011; Shprits and Ni et al., 2009) which solves equations (2), (3), and the solution of a cold plasma dispersion relation. Input parameters are derived from spacecraft measurements when possible. Electron number density is 960 cm^{-3} as derived from EMFISIS measurements. Wave shape is found from a Gaussian fit of the form $\exp(-[\mathrm{f}-\mathrm{f_m}]/\delta f)^2$ to the time-averaged power near 4:45 UT which fulfills EMIC wave criteria with the parameters $\mathrm{f_m}$ = 0.57 Hz and δf = 0.045 Hz (shown in the Supporting Information). The local equatorial magnetic field strength is found to be 647 nT from EMFSIS measurements. The local plasma composition is taken to be 70% H+, 20% He+, and 10% O+ as found by Meredith et al., (2003) and as used for similar diffusion coefficient calculations (e.g., Summers & Thorne, 2003; Usanova et al., 2014). The EMIC waves are assumed to be confined within ±15° as consistent with observations of other EMIC wave events (Chen et al., 2019, Saikin et al., 2015). The wave normal angle is assumed to have a quasi-parallel distribution (e.g., Ni et al., 2015). The effects of polarization reversal are not considered here (e.g., Cao et al., 2020). We here consider orders of cyclotron resonance from -5 to 5. The EMIC waves are assumed to be left-hand polarized as considered for prior EMIC wave diffusion coefficient theory (Summers et al., 2007) and as observed for EMIC waves observed at higher L* values during the event, shown in Figure 3. Two different cases are evaluated for the diffusion coefficients due to EMIC waves at L* = 3.5 in the absence of their direct observation, scaling the frequency of the nearby observed wave power to the time when the spacecraft crosses L* = 3.5 using the local magnetic field strength, or assuming similar waves as those observed at higher L* values. These two cases are presented in this study: First, we consider He+ band EMIC waves, which are the band in which EMIC wave power is observed during the satellite orbit of loss as shown in Figure 3. The frequency range of the wave spectrum is normalized to the time when the spacecraft passes L* = 3.5 based on measurements of the magnetic field strength during 04:38:40 – 04:49:56 UT. This normalization is done by scaling the central frequency of the wave and the wave power spectral width such that the ratio of these parameters to the He+ frequency band are the same as the observations of the nearby EMIC wave power. Second, we normalize the frequency range of the spectrum based on a magnetic field strength of 647 nT. This frequency range of the spectrum is located mainly in the O+ band when the spacecraft is in the region near L* = 3.5, thus the waves are treated as O+ band EMIC waves with an upper frequency limit of 0.99 times the local O+ gyrofrequency. This allows for the consideration and comparison of the effects of He+ and O+ band EMIC waves during the event with realistic wave parameters as observed during the satellite orbit of interest, as no EMIC waves are directly observed during the spacecraft crossing of L* = 3.5 during which the rapid PSD loss is observed.

The minimum resonant energies and pitch angle diffusion coefficients for each of these cases are shown in Figure 4. Minimum resonant energies are indicated by the minimum energy at which the diffusion coefficient is defined at a given pitch angle, the waves do not resonate with electrons at energies where the diffusion coefficient is not defined. The value of the pitch angle diffusion coefficient is indicated by the color scale in Figure 4. The calculated energy and cross diffusion terms are multiple orders of magnitude less than the calculated pitch angle diffusion coefficients; we will focus only on the effects of pitch angle diffusion here. The dispersion relationship results, explicit resonant regions, and energy and cross diffusion terms are shown in the Supporting Information. Panel A shows the results for He+ band EMIC waves, and that they do not resonate with electrons less than 56 MeV at α_{eq} = 54° (which corresponds to K = 0.10

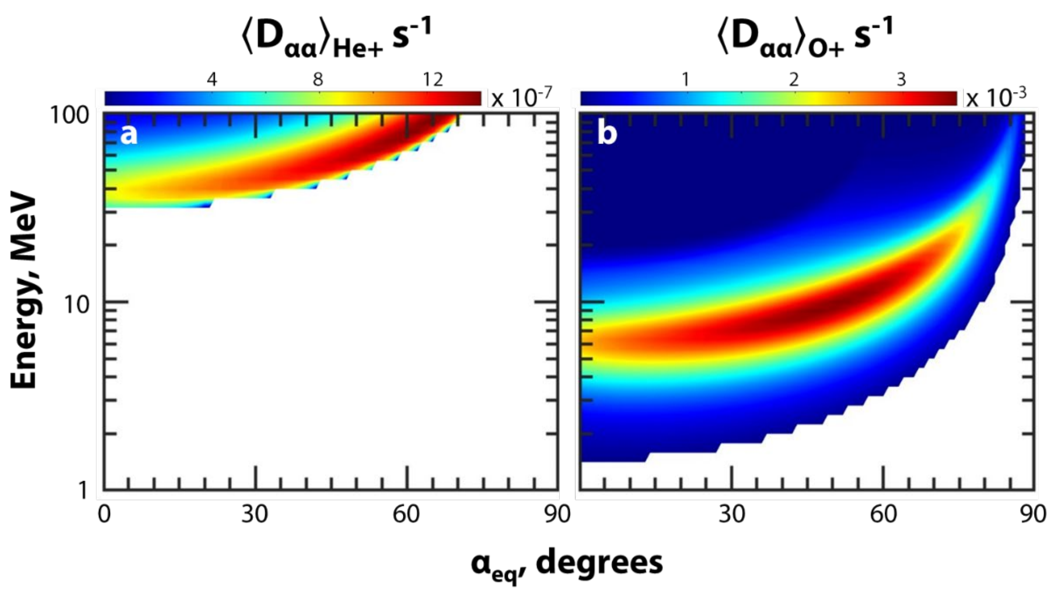

Figure 4 Panel a: minimum resonant energy and bounce-averaged diffusion coefficient calculated for He+ band EMIC waves with the described input parameters. Minimum resonant energies are the lowest energy at each pitch angle for which the diffusion coefficient is defined. The strength of the diffusion coefficient is indicated by the color bar on top of the plot. Panel b: Same as left, but for O+ band EMIC waves.

$G^{1/2}R_E$ at L* = 3.5 during this event), much higher than the energies where loss is observe. In panel b, we show that representative O+ band EMIC waves can resonate with electrons down to 2.8 MeV energies at $\alpha_{eq} = 54°$, encompassing the electron energies observed to decrease during this event of study. The diffusion coefficients due to O+ band waves are also much larger – about 4 orders of magnitude greater when comparing peak values in the energy ranges presented here. We also show in Figure 4 that the diffusion coefficient increases with increasing electron energy from ~MeV to several MeV, which matches the behavior of the loss mechanism observed and shown in Figure 1.

To model the effects of these diffusion coefficients on electron PSD we use a one-dimensional pitch angle diffusion model (equation 4) (e.g., Ni et al., 2015). Boundary conditions for modeled PSD f are $df/dt(\alpha_{eq} = 90°) = 0$ and $f(\alpha_{eq} < \alpha_{loss\ cone}) = 0$. The first condition is an upper boundary condition stating that there should not be any change in PSD for particles that are perfectly trapped, and the second condition defines that PSD within the loss cone should exhibit rapid loss during the simulation. We assume the initial PSD profile follows a sine function in equatorial pitch angle (e.g., Ni et al., 2013, 2015). We match the prescription of initial PSD to the PSD observations from RBSP A shown in Figure 1, noting that the observations shown in Figure 1 are for second adiabatic invariant K = 0.10 $G^{1/2}R_E$ which corresponds to $\alpha_{eq} = 54°$ at L* = 3.5 during this event. PSD evolution is simulated by solving equation (1) over one 9-hour satellite orbit and shown in Figure 5 for the 3000 MeV/G population, which corresponds to ~5 MeV electrons at L* = 3.5 and K = 0.10 $G^{1/2}R_E$. We assume EMIC waves are present for 2% of

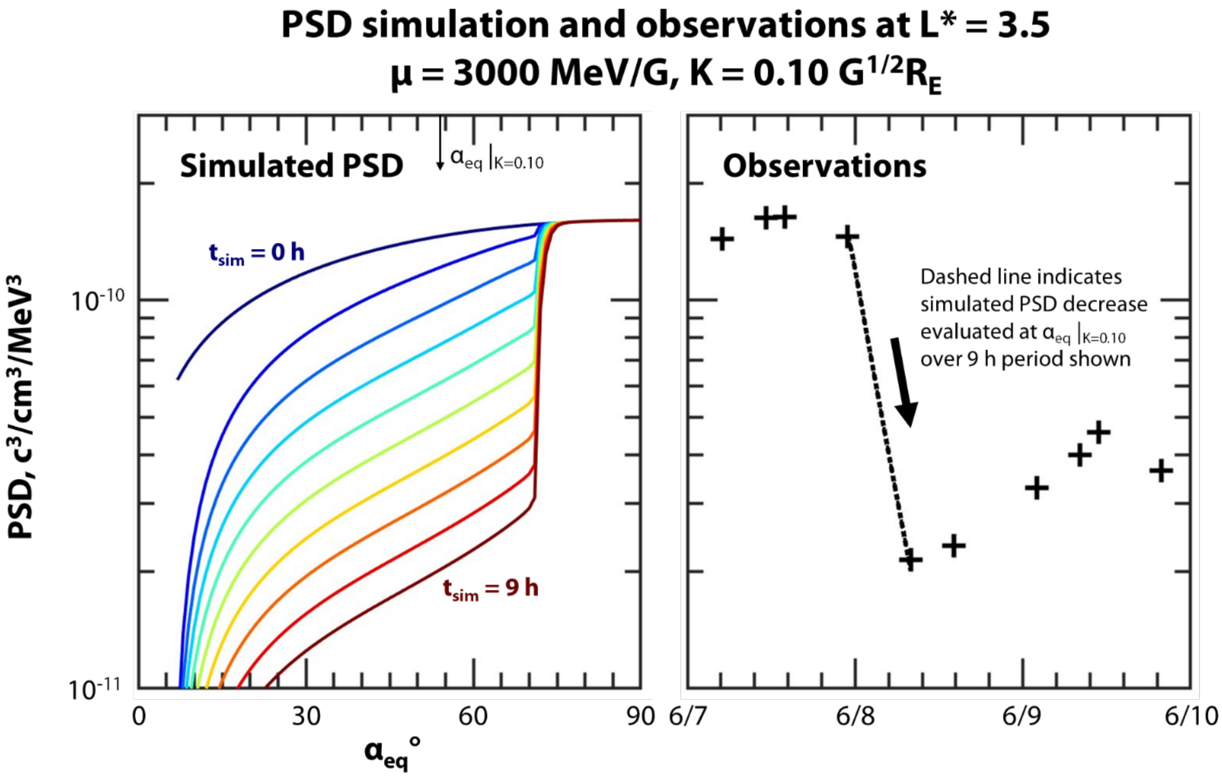

Figure 5 Left: simulated PSD for μ = 3000 MeV/G, K = 0.10 $G^{1/2}R_E$ electrons using the pure pitch angle diffusion model described in the text. The pitch angle corresponding to K = 0.10 $G^{1/2}R_E$ is indicated on the top x-axis, and the initial PSD value at this pitch angle is prescribed to match the observed PSD by Van Allen Probe A immediately before the observed loss at L* = 3.5. The evolution of PSD is plotted every hour and progresses from blue to red for 9-hours. Right: Pass-averaged PSD from Van Allen Probe A for μ = 3000 MeV/G, K = 0.10 $G^{1/2}R_E$ electrons at L* = 3.5 plotted with + marks for 7 through 9 June 2015. Simulated PSD (shown on the left) is evaluated at the pitch angle corresponding to K = 0.10 $G^{1/2}R_E$ and shown with a dashed line, starting from the satellite pass point used for initial conditions for the PSD simulation.

the drift orbit of the electrons, similar to MLT drift orbit averaging assumed by other studies (e.g., Summers et al., 2007) and agreeing with the occurrence rate ranges of O+ band EMIC waves at L* = 3.5 (Chen et al., 2019; Saikin et al., 2015). These simulation results are shown in the left panel of Figure 5. The initial spectrum of PSD is shown in blue, for we prescribe such that the PSD at $\alpha_{eq} = 54°$ agrees with the observations from Van Allen Probe A from the pass immediately before the rapid decrease in PSD. We plot PSD spectra progression every hour with color progressing from red to blue. Results in Figure 5 are for μ = 3000 MeV/G electrons over 9-hours, which is one satellite orbit, the amount of time during which Van Allen Probe A observes rapid PSD loss. This simulation result in Figure 5 shows the significant and fast decrease in PSD at $\alpha_{eq} \lesssim 70°$, and the narrowing of the pitch angle spectra over the course of the satellite orbit simulated. In the right panel of Figure 5, we compare this simulation result (dashed line) with the observed PSD from Van Allen Probe A from 7 through 9 June 2015. Observed PSD at L* = 3.5, K = 0.10 $G^{1/2}R_E$ is shown for each satellite pass and indicated by + marks. Evaluating the simulation result at $\alpha_{eq} = 54°$, we show here good agreement between the simulated PSD loss due to EMIC wave effects and the observations, under the simulation conditions and diffusion coefficients found as described.

Results shown in Figure 5 are for 3000 MeV/G electrons and show a decrease by a factor of 7.2, compared to observational decrease of 6.8 over a 9-hour period. Similar analysis is done for the 1500, 2000, and 2500 MeV/G populations, for which we report respective decreases by factors of 2.8, (3.2 observed), 3.6 (4.5 observed), 5.0, (6.5 observed), 7.2 (6.8 observed) for these populations over the 9-hour period. These results for all μ values are shown in the Supporting Information.

5. Discussion

The calculation of diffusion coefficients for representative EMIC waves during the event as shown in Figure 4 indicates that EMIC waves in the O+ band and not the He+ band can be driving the loss of electrons at multi-MeV energies as shown in Figure 1. We modeled PSD evolution using these EMIC wave effects and pure pitch angle diffusion. The results in Figure 5 show decrease of PSD at lower pitch angles while preserving the populations at higher pitch angles, thus narrowing the pitch angle spectra, as observed during the event and shown in Figure 5. O+

band EMIC waves are less common than He+ band EMIC waves as found by studies of EMIC observations from the Van Allen Probes era (Sigsbee et al., 2023, Chen et al., 2019, Yu et al., 2015); however, when O+ EMIC waves are observed, they are most prevalent in the range $3 < L < 4$, which is the region where this loss is observed, and are as common as H+ EMIC waves in this region (Chen et al., 2019; Saikin et al., 2015). The dwell time of the spacecraft decreases with L value (as shown by Chen et al., 2019; Sigsbee et al., 2023; Yu et al., 2015) decreasing the likelihood of observing EMIC wave structures in this region. Studies by Yu et al., (2015) of the early Van Allen Probes era (2012-2014) suggest that O+ EMIC waves are found generally in the outer plasmasphere and occasionally the plasma trough which is the region in which this loss process is observed. In this region the O+ density can be higher than the partial ion compositions used here, thus increasing the strength of O+ band EMIC waves. A study of Van Allen Probes data from 2012-2017 by Chen et al., (2019) shows that O+ band waves do occur mostly in the region 3-3.5 R_E, which corresponds to this region of loss. This study also showed that O+ band EMIC waves are observed to have small wave normal angles and linear polarization as assumed here. EMIC waves can be bursty and occur on short timescales making them difficult to be fully measured in time and space even by a two-spacecraft mission, but EMIC effects can be observed in these multi-MeV electrons which have drift periods on the timescale of minutes and transport information about the waves to the satellite for measurement. O+ band waves specifically are thought to happen near the plasmapause boundary where the oxygen torus (e.g., Nose et al., 2015) expands and leads to growth of O+ band waves in this region (Yu et al., 2015). During the event of study, no appreciable O+ density increase was shown using partial ion densities as found from the Helium, Oxygen, Proton, and Electron (HOPE) instrument, or from inferred ion densities down to >eV energies using the methods of Goldstein et al., (2013), as shown in the Supporting Information. Therefore, it is not clear that the oxygen torus is present during this event.

Minimum resonant energies and the strength of diffusion coefficients from EMIC wave effects will vary due to the temperature of the ions and the local ion composition, as seen in equations (1) and (2). Here, we have assumed a cold plasma, and the solution of a cold plasma dispersion relation is used for computing the results of equations (1) and (2) as developed by Summers & Thorne (2003) and Summers et al., (2007). Sensitivity of the solutions of plasma dispersion relations when using cold, warm, or hot plasma dispersion relations have been discussed in previous studies, and have been shown to affect the solution by changing the wave number solution which changes the resonant conditions (e.g., Bashir et al., 2021, 2022; Lee et al., 2014). However, these observations and modeling in this study are made at low L* values where the local number density is near 1000 cm^{-3} and within the plasmapause. Therefore, a cold plasma approximation is an accurate assumption for the solutions of (1) and (2). Similar use of the cold plasma dispersion relation has been used for calculating diffusion coefficients for EMIC waves up to L* = 4.5 (Usanova et al., 2014).

Ion compositions must also be assumed due to the lack of direct in-situ measurements. In certain events when EMIC waves are observed in multiple bands, one can estimate the local ion compositions (e.g., Min et al., 2015; Qin et al., 2019). However, in the event of study, only one band is shown, and at higher L* values than where the observed loss feature occurs. Therefore, the local ion composition must be assumed. The solution of the plasma dispersion relation is sensitive to the local ion composition (e.g., Bashir et al., 2021, 2022; Summers et al., 2007). The assumed compositions found by Meredith et al., (2003) however provide adequate representative parameters for the local ion compositions and have been used for similar studies of diffusion coefficients from EMIC waves (e.g., Usanova et al., 2014). Furthermore, the minimum resonant energy does not vary as strongly with ion composition as it does with other parameters (such as local number density, which is inferred from satellite measurements during the event). Significant deviation from statistically found average EMIC wave characteristics and ion compositions would be required for He+ band waves to affect the populations where loss is observed, therefore it is more likely here that O+ band waves are affecting these multi-MeV electrons at L* = 3.5 than He+ band waves.

Here we have only modeled the effects of L-mode quasi-linear EMIC waves. Other studies acknowledge that often the combined effects of EMIC waves with other waves such as chorus or hiss waves chorus and/or hiss waves are required to produce loss of the entire pitch angle spectra to fully match observations of loss at high α_{eq} (Drozdov et al., 2020; Qin et al., 2019; Ross et al., 2021). We show here that EMIC wave effects can account for the loss in PSD shown and can induce narrowing of the pitch angle spectra, but that other loss mechanisms must be present to affect the dynamics of higher pitch angle electrons, PSD at high pitch angles remain constant in our simulations as shown in Figure 5 due to the lack of a defined pitch angle diffusion coefficient at that region for the electron populations of study. Hiss waves are prevalent within the plasmapause can scatter particles to the pitch angles where they can then be affected by EMIC waves (e.g., Drozdov et al., 2020; Li et al., 2007). The loss feature at L* = 3.5 is shown to be within the plasmapause here as shown here. A study of multi-MeV electron flux data from the Van Allen Probes in 2015 by Ross et al., (2021) suggested that hiss wave and EMIC waves are both required to reproduce observed loss at L* ≤ 3.75. While their study did not include O+ band EMIC waves due to their low occurrence rate, we show here that representative O+ band waves alone can account for large loss in multi-MeV electron PSD on rapid timescales during the event of study.

Other governing factors of the simulation space may be found to affect the L* dependence of local minimums in PSD. Preconditioning of the system may be important for these structures, as EMIC wave effects are generally most prevalent when the wave first interacts with the dense plasmasphere (e.g., Usanova et al., 2021). Compression of the plasmapause may be necessary for EMIC wave effects to cause local minimums in multi-MeV electrons at lower L* values, such as during the strong storm in March 2015 before this observation (Dst_{min} = -234). During the period after the March 2015 storm through June 2015, Hogan et al., (2021) show the development of the local minimum at L* = 3.5 discussed here. During this period and before the 8 June event studied in detail here, other moderate storms in terms of Dst are present: 10-11 April (Dst_{min} = -85 nT), 15-19 April (Dst_{min} = -88 nT), and 11-13 May (Dst_{min} = -82 nT). Decay of PSD at L* = 3.5 during these events contributes to local loss but not the formation of a local minimum in PSD, only during the 8 June event is the PSD low enough at L* = 3.5 that a minimum can then form. Loss during these events prior moderate events may have been preferential at L* = 3.5 as well, and perhaps governed by the same mechanisms as those discussed here, as EMIC waves are most effective at causing loss when first crossing the plasmapause, regardless of wave band. While continuous O+ band waves are unlikely due to their infrequent observations, it is possible that EMIC waves in the He+ or H+ bands are causing local loss during these prior storms, or other mechanisms not revealed in this event study are present. Hiss waves also affect multi-MeV electrons on these multi-month timescales and may play a part in the preconditioning of PSD at L* = 3.5 for the 8 June 2015 event as well. This topic warrants future research as the loss at certain L* values can lead to the formation of the third radiation belt and significantly affect dynamics of the radiation belt structure, and here, driving mechanisms of uncommon wave types (O+ band EMIC waves) are shown to be able to be capable of causing this feature during only a moderate geomagnetic storm in terms of Dst (Dst_{min} = -67 nT) under the given preconditioning. Therefore, future study is required.

6. Conclusions

1. Rapid loss of multi-MeV electron PSD is shown during a moderate storm with minimum Dst = -67 nT. This loss is primarily at L* = 3.5 and causes a local PSD minimum to form within one satellite orbit. The loss is shown to be energy dependent, with increasing prominence of the local minimum with increasing μ.
2. Pitch angle bite outs are shown in multi-MeV electron flux channels from the REPT instrument during this event, indicating narrowing of the pitch angle distribution and a loss mechanism that affects multi-MeV electrons most strongly at lower pitch angles.
3. Quasi-linear theory is used to analyze the effects of He+ and O+ band waves for the plasma environment at L* = 3.5 during the event. Analysis of minimum resonant energies due to each wave type show O+ band waves as a possible driver of multi-MeV electron dynamics. Representative O+ band EMIC wave effects are simulated in a one-dimensional pitch angle diffusion model of PSD using initial conditions observed during the event and calculated diffusion coefficients. These simulation results show that O+ band EMIC waves can produce loss rates similar to the observed multi-MeV PSD loss at L* = 3.5 in one satellite orbit.

Acknowledgements

REPT data and RBSP Magnetic Ephemeris data are provided by the Energetic Particle, Composition, and Thermal Plasma Suite (ECT) (Spence et al., 2013). We thank the REPT team (Baker et al., 2012) as well as the EMFISIS team (Kletzing et al., 2013) for use of their respective instrument data. ECT data used in this study is available from https://rbsp-ect.newmexicoconsortium.org/data_pub/. EMFISIS data are is available from the NASA OMNI web database: https://omniweb.gsfc.nasa.gov/. Plasmapause location determined from local number density measurements by Craig Kletzing is available at https://emfisis.physics.uiowa.edu/Events/rbsp-a/plasmapause/. Dst values are provided by Kyoto University: wdc.kugi.kyoto-u.ac.jp. The authors thank Alexander Drozdov and Mary Hudson for valuable discussions regarding this work. This work has been supported in part by NSF grant AGS 1834971, NASA grants NSSC19K0237, 80NSSC20K0913, and 80NSSC21K0583. NASA/RBSP-ECT funding is from JHU/APL contract 967399 under prime NASA contract NAS5-01072. H. Zhao is supported by NSF grant AGS 2140933, 2131012, 2247857, and NASA grant 80NSSC22K0473.

References

Aseev, N. A., et al. "Signatures of Ultrarelativistic Electron Loss in the Heart of the Outer Radiation Belt Measured by Van Allen Probes." *Journal of Geophysical Research: Space Physics*, vol. 122, no. 10, 2017, https://doi.org/10.1002/2017ja024485.

Bashir, M. F., Artemyev, A., Zhang, X.-J., & Angelopoulos, V. (2022). Energetic electron precipitation driven by the combined effect of ULF, EMIC, and whistler waves. Journal of Geophysical Research: Space Physics, 127, e2021JA029871. https://doi.org/10.1029/2021JA029871

Bashir, M. F., Artemyev, A., Zhang, X.-J., & Angelopoulos, V. (2022). Hot plasma effects on electron resonant scattering by electromagnetic ion cyclotron waves. Geophysical Research Letters, 49, e2022GL099229. https://doi. org/10.1029/2022GL099229

Baker, D. N., et al. "The Relativistic Electron-Proton Telescope (REPT) Instrument on Board the Radiation Belt Storm Probes (RBSP) Spacecraft: Characterization of Earth's Radiation Belt High-Energy Particle Populations." *Space Science Reviews*, vol. 179, no. 1-4, 2012, pp. 337–381., https://doi.org/10.1007/s11214-012-9950-9.

Baker DN, Kanekal SG, Hoxie VC, Henderson MG, Li X, Spence HE, Elkington SR, Friedel RH, Goldstein J, Hudson MK, Reeves GD, Thorne RM, Kletzing CA, Claudepierre SG. A long-lived relativistic electron storage ring embedded in Earth's outer Van Allen belt. Science. 2013 Apr 12;340(6129):186-90. doi: 10.1126/science.1233518. Epub 2013 Feb 28. PMID: 23450000.

Barker, A. B., Li, X., & Selesnick, R. (2005). Modeling the radiation belt electrons with radial diffusion driven by the solar wind. Space Weather, 3, S10003. https://doi.org/10.1029/2004SW000118

Bingley, L., Angelopoulos, V., Sibeck, D., Zhang, X., Halford, A. The evolution of a pitch-angle "bite-out" scattering signature caused by EMIC wave activity: a case study. J. Geophys. Res. Space Phys. 124, 5042–5055 (2019). https://doi.org/10.1029/2018JA026292

Bortnik, J., et al. "An Automatic Wave Detection Algorithm Applied to PC1 Pulsations." *Journal of Geophysical Research: Space Physics*, vol. 112, no. A4, 2007, https://doi.org/10.1029/2006ja011900.

Cao, Xing, et al. "Effects of Polarization Reversal on the Pitch Angle Scattering of Radiation Belt Electrons and Ring Current Protons by Emic Waves." *Geophysical Research Letters*, vol. 47, no. 17, 2020, https://doi.org/10.1029/2020gl089718.

Cervantes, S., et al. "Quantifying the Effects of Emic Wave Scattering and Magnetopause Shadowing in the Outer Electron Radiation Belt by Means of Data Assimilation." Journal of Geophysical Research: Space Physics, vol. 125, no. 8, 2020, https://doi.org/10.1029/2020ja028208.

Chen, Y., et al. "Phase Space Density Distributions of Energetic Electrons in the Outer Radiation Belt during Two Geospace Environment Modeling Inner Magnetosphere/Storms Selected Storms." *Journal of Geophysical Research*, vol. 111, no. A11, 2006, https://doi.org/10.1029/2006ja011703.

Chen, H., Gao, X., Lu, Q., & Wang, S. (2019). Analyzing EMIC waves in the inner magnetosphere using long-term Van Allen Probes observations. Journal of Geophysical Research: Space Physics, 124, 7402–7412. https://doi.org/ 10.1029/2019JA026965

Drozdov, A. Y., Aseev, N., Effenberger, F., Turner, D. L., Saikin, A., & Shprits, Y. (2019). Storm time depletions of multi-MeV radiation belt electrons observed at different pitch angles. Journal of Geophysical Research: Space Physics, 124, https://doi.org/10.1029/2019JA027332

Drozdov, A. Y., et al. "Depletions of Multi-Mev Electrons and Their Association to Minima in Phase Space Density." Geophysical Research Letters, vol. 49, no. 8, 2022, https://doi.org/10.1029/2021gl097620.

Drozdov, A. Y., et al. "The Role of Hiss, Chorus, and Emic Waves in the Modeling of the Dynamics of the Multi-MeV Radiation Belt Electrons." (2020) Journal of Geophysical Research: Space Physics, vol. 125, no. 9, 2020, https://doi.org/10.1029/2020ja028282.

Fraser, B.J. Observations of ion cyclotron waves near synchronous orbit and on the ground. Space Sci Rev 42, 357–374 (1985). https://doi.org/10.1007/BF00214993

Goldstein, J., De Pascuale, S., Kletzing, C., Kurth, W., Erickson, P. J., Foster, J. C., Genestreti, K., Skoug, R. M., Larsen, B. A., Kistler, L. M., Mouikis, C., & Spence, H. (2014). Simulation of Van Allen Probes plasmapause encounters. Journal of Geophysical Research: Space Physics, 119, 7464– 484. https://doi.org/10.1002/2014JA020252

Green, Janet C and Kivelson. "Relativistic Electrons in the Outer Radiation Belt: Differentiating between Acceleration Mechanisms." *Journal of Geophysical Research*, vol. 109, no. A3, 2004, https://doi.org/10.1029/2003ja010153.

Hogan, Benjamin, et al. "Multi-MeV Electron Dynamics near the Inner Edge of the Outer Radiation Belt." *Geophysical Research Letters*, vol. 48, no. 23, 2021, https://doi.org/10.1029/2021gl095455.

Thorne, R. M., & Kennel, C. F. (1971). Relativistic electron precipitation during magnetic storm main phase. Journal of Geophysical Research, 76(19), 4446–4453. https://doi.org/10.1029/JA076i019p04446

Kim, H. J., & Chan, A. A. (1997). Fully adiabatic changes in storm time relativistic electron fluxes. Journal of Geophysical Research: Space Physics, 102(A10), 22107–22116. https://doi.org/10.1029/97ja01814

Kletzing, C. A., et al. "The Electric and Magnetic Field Instrument Suite and Integrated Science (EMFISIS) on RBSP." *Space Science Reviews*, vol. 179, no. 1-4, 2013, pp. 127–181., https://doi.org/10.1007/s11214-013-9993-6.

Lee, J. H., and Angelopoulos, V. (2014), Observations and modeling of EMIC wave properties in the presence of multiple ion species as function of magnetic local time, J. Geophys. Res. Space Physics, 119, 8942– 8970, doi:10.1002/2014JA020469.

Lenchek, A., S. Singer, and R. Wentworth (1961), Geomagnetically trapped electrons from cosmic ray albedo neutrons, J. Geophys. Res., 66(12), 4027–4046, doi:10.1029/JZ066i012p04027.

Lejosne, S., and Kollmann, P. (2020), Radiation Belt Diffusion at Earth and Beyond. *Space Science Reviews*. https://doi.org/10.1007/s11214-020-0642-6

Li, W., Shprits, Y. Y., & Thorne, R. M. (2007). Dynamic evolution of energetic outer zone electrons due to wave-particle interactions during storms. Journal of Geophysical Research, 112, A10220. https://doi.org/10.1029/2007JA012368

Li, X., Baker, D. N., Temerin, M., Cayton, T. E., Reeves, E. G. D., Christensen, R. A., et al. (1997). Multisatellite observations of the outer zone electron variation during the November 3–4, 1993, magnetic storm. Journal of Geophysical Research: Space Physics, 102(A7), 14123–14140. https://doi.org/10.1029/97ja01101

Li, W., & Hudson, M. K. (2019). Earth's Van Allen radiation belts: From discovery to the Van Allen Probes era. *Journal of Geophysical Research: Space Physics*, 124, 8319– 8351. https://doi.org/10.1029/2018JA025940

Malaspina, D. M., Jaynes, A. N., Boulé, C., Bortnik, J., Thaller, S. A., Ergun, R. E., & Wygant, J. R. (2016). The distribution of plasmaspheric hiss wave power with respect to plasmapause location. Geophysical Review Letters, 43, 7878–7886. https://doi.org/10.1002/2016GL069982

Mauk, B. H., et al. "Science Objectives and Rationale for the Radiation Belt Storm Probes Mission." (2012) *Space Science Reviews*, vol. 179, no. 1-4, 2012, pp. 3–27., https://doi.org/10.1007/s11214-012-9908-y.

Meredith, N. P., Horne, R. B., & Anderson, R. R. (2001). Substorm dependence of chorus amplitudes: Implications for the acceleration of electrons to relativistic energies. Journal of Geophysical Research, 106, 13165– 13178. https://doi.org/10.1029/2000JA900156

Meredith, Nigel P. "Statistical Analysis of Relativistic Electron Energies for Cyclotron Resonance with Emic Waves Observed on CRRES." *Journal of Geophysical Research*, vol. 108, no. A6, 2003, https://doi.org/10.1029/2002ja009700.

Min, K., Liu, K., Bonnell, J., Breneman, A., Denton, R., Funsten, H., et al. (2015). Study of EMIC wave excitation using direct ionmeasurements.Journal of Geophysical Research: Space Physics,120, 2702–2719

McIlwain, C. E. (1961). Coordinates for mapping the distribution of magnetically trapped particles. Journal of Geophysical Research, 66(11), 3681–3691. https://doi.org/10.1029/jz066i011p03681

Ni, B., R. M. Thorne, Y. Y. Shprits, and J. Bortnik (2008), Resonant scattering of plasma sheet electrons by whistler-mode chorus: Contribution to diffuse auroral precipitation, Geophys. Res. Lett., 35, L11106, doi:10.1029/2008GL034032.

Ni, B., R. M. Thorne, N. P. Meredith, R. B. Horne, and Y. Y. Shprits (2011), Resonant scattering of plasma sheet electrons leading to diffuse auroral precipitation: 2. Evaluation for whistler mode chorus waves, J. Geophys. Res., 116, A04219, doi:10.1029/2010JA016233.

Ni, B., J. Bortnik, R. M. Thorne, Q. Ma, and L. Chen (2013), Resonant scattering and resultant pitch angle evolution of relativistic electrons by plasmaspheric hiss, J. Geophys. Res. Space Physics, 118, 7740–7751, doi:10.1002/2013JA019260.

Ni, B., et al. (2015), Resonant scattering of outer zone relativistic electrons by multiband EMIC waves and resultant electron loss time scales, J. Geophys. Res. Space Physics, 120, 7357–7373, doi:10.1002/2015JA021466

Ni, B., Huang, H., Zhang, W., Gu, X., Zhao, H., Li, X., et al. (2019). Parametric sensitivity of the formation of reversed electron energy spectrum caused by plasmaspheric hiss. Geophysical Research Letters, 46(8), 4134–4143. https://doi.org/10.1029/2019gl082032

Nosé, M., Oimatsu, S., Keika, K., Kletzing, C. A., Kurth, W. S., De Pascuale, S., et al. (2015). Formation of the oxygen torus in the inner magnetosphere: Van Allen Probes observations. Journal of Geophysical Research: Space Physics, 120(2), 1182–1196. https://doi.org/10.1002/2014JA020593

Orlova K., Y. Shprits, (2014), Model of lifetimes of the outer radiation belt electrons in a realistic magnetic field using realistic chorus wave parameters, J. Geophys. Res. [Space Physics], 119, 770-780, doi:10.1002/2013JA019596

Qin, M., Hudson, M. K., Li, Z., Millan, R. M., Shen, X.-C., Shprits, Y. Y., et al. (2019). Investigating loss of relativistic electrons associated with EMIC waves at low L values on

22 June 2015. Journal of Geophysical Research: Space Physics, 124, 4022–4036. https://doi. org/10.1029/2018JA025726

Roederer, J. G. "Dynamics of Geomagnetically Trapped Radiation." *Physics and Chemistry in Space*, 1970, https://doi.org/10.1007/978-3-642-49300-3.

Roederer, J. G., & Lejosne, S. (2018). Coordinates for representing radiation belt particle flux. Journal of Geophysical Research: Space Physics,123, 1381- 1387. https://doi.org/10.1002/2017JA025053

Ross, J. P. J., Glauert, S. A., Horne, R. B., Watt, C. E. J., & Meredith, N. P. (2021). On the variability of EMIC waves and the consequences for the relativistic electron radiation belt population. Journal of Geophysical Research: Space Physics, 126, e2021JA029754. https://doi. org/10.1029/2021JA029754

Saikin, A. A., et al. "The Occurrence and Wave Properties of H + -, He + -, and O + -Band Emic Waves Observed by the Van Allen Probes." *Journal of Geophysical Research: Space Physics*, vol. 120, no. 9, 2015, pp. 7477–7492., https://doi.org/10.1002/2015ja021358.

Selesnick, R. S. "Atmospheric Losses of Radiation Belt Electrons." *Journal of Geophysical Research*, vol. 108, no. A12, 2003, https://doi.org/10.1029/2003ja010160.

Shprits, Y. Y., and B. Ni (2009), Dependence of the quasi-linear scattering rates on the wave normal distribution of chorus waves, J. Geophys. Res., 114, A11205, doi:10.1029/2009JA014223.

Shprits et al., 2016, Wave-induced loss of ultra-relativistic electrons in the Van Allen radiation belts, DOI: 10.1038/ncomms12883

Shprits, Y. Y., A. Kellerman, N. Aseev, A. Y. Drozdov, and I. Michaelis (2017), Multi-MeV electron loss in the heart of the radiation belts, Geophys. Res. Lett., 44, 1204–1209, doi:10.1002/ 2016GL072258.Schulz, Michael, and Louis J. Lanzerotti. "Particle Diffusion in the Radiation Belts." *Physics and Chemistry in Space*, 1974, https://doi.org/10.1007/978-3-642-65675-0.

Sigsbee, K., Kletzing, C. A., Faden, J., & Smith, C. W. (2023). Occurrence rates of electromagnetic ion cyclotron (EMIC) waves with rising tones in the Van Allen Probes data set. Journal of Geophysical Research: Space Physics, 128, e2022JA030548. https://doi. org/10.1029/2022JA030548

Spence, H. E., Reeves, G. D., Baker, D. N., Blake, J. B., Bolton, M., Bourdarie, S., et al. (2013). Science goals and overview of the radiation belt storm probes (RBSP) energetic particle, composition, and thermal plasma (ECT) suite on NASA's van allen Probes mission. Space Science Reviews, 179(1), 311–336. https://doi.org/10.1007/s11214-013-0007-5Summers & Thorne, (2003), Relativistic electron pitch-angle scattering by electromagnetic ion cyclotron waves during geomagnetic storms. Journal of Geophysical Research, Vol 108, N. A4, 1143, doi:10.1029/2002JA009489

Thorne, R. M., and Kennel, C.F (1971). Relativistic electron precipitation during magnetic storm main phase. Journal of Geophysical Research, Vol 76, Issue 19, 4446-4453. https://doi.org/10.1029/JA076i019p04446

Thorne, R. M. (2010). Radiation belt dynamics: The importance of wave-particle interactions. Geophysical Research Letters, 37, L22107. https://doi.org/10.1029/2010GL044990

R.M. Thorne, W. Li, B. Ni, Q. Ma, J. Bortnik, D.N. Baker, H.E. Spence, G.D. Reeves, M.G. Henderson, C.A. Kletzing, W.S. Kurth, G.B. Hospodarsky, D. Turner, V. Angelopoulos, Evolution and slow decay of an unusual narrow ring of relativistic electrons near L ∼ 3.2

following the September 2012 magnetic storm. Geophys. Res. Lett. 40(1-5), 3507–3511 (2013a). https://doi.org/10.1002/grl.50627

Tsyganenko, N. A., & Sitnov, M. I. (2005). Modeling the dynamics of the inner magnetosphere during strong geomagnetic storms. *Journal of Geophysical Research*, **110**, A03208. https://doi.org/10.1029/2004JA010798

Turner, D. L., Angelopoulos, V., Morley, S. K., Henderson, M. G., Reeves, G. D., Li, W., et al. (2014). On the cause and extent of outer radiation belt losses during the 30 September 2012 dropout event. Journal of Geophysical Research: Space Physics, 119(3), 1530–1540. https://doi. org/10.1002/2013ja019446

Su, Z., Gao, Z., Zheng, H., Wang, Y., Wang, S., Spence, H.E., Reeves, G.D., Baker, D.N., Wygant, J.R., Rapid loss of radiation belt relativistic electrons by EMIC waves. J. Geophys. Res. Space Phys. 122, 10 (2017). https://doi.org/10.1002/2017ja024169

Summers, D., and R. M. Thorne, Relativistic electron pitch-angle scattering by electromagnetic ion cyclotron waves during geomagnetic storms, J. Geophys. Res.,108(A4), 1143, doi:10.1029/2002JA009489, 2003

Summers, D., B. Ni, and N. P. Meredith (2007), Timescales for radiation belt electron acceleration and loss due to resonant wave-particle interactions: 1. Theory, J. Geophys. Res., 112, A04206, doi:10.1029/2006JA011801.

Usanova, M. E., I. R. Mann, J. Bortnik, L. Shao, and V. Angelopoulos (2012), THEMIS observations of electromagneticion cyclotron wave occurrence: Dependence on AE, SYMH, and solar wind dynamic pressure, J. Geophys. Res.,117, A10218, doi:10.1029/2012JA018049

Usanova, M. E., et al. "Effect of Emic Waves on Relativistic and Ultrarelativistic Electron Populations: Ground-Based and Van Allen Probes Observations." *Geophysical Research Letters*, vol. 41, no. 5, 2014, pp. 1375–1381., https://doi.org/10.1002/2013gl059024.

Usanova ME (2021) Energy Exchange Between Electromagnetic Ion Cyclotron (EMIC) Waves and Thermal Plasma: From Theory to Observations. Front. Astron. Space Sci. 8:744344. doi: 10.3389/fspas.2021.744344

Xiang, Zheng, et al. "Understanding the Mechanisms of Radiation Belt Dropouts Observed by Van Allen Probes." *Journal of Geophysical Research: Space Physics*, vol. 122, no. 10, 2017, pp. 9858–9879., https://doi.org/10.1002/2017ja024487.

Xiang, Z., Tu, W., Ni, B., Henderson, M. G., & Cao, X. (2018). A statistical survey of radiation belt dropouts observed by Van Allen Probes. Geophysical Research Letters, 45, 8035–8043. https://doi.org/ 10.1029/2018GL078907

Yu, X., Z. Yuan, D. Wang, H. Li, S. Huang, Z. Wang, Q. Zheng, M. Zhou, C. A. Kletzing, and J. R. Wygant (2015), In situ observations of EMIC waves in O+ band by the Van Allen Probe A, Geophys. Res. Lett., 42, 1312–1317, doi:10.1002/ 2015GL063250.

Zhao, H., Ni, B., Li, X., Baker, D. N., Johnston, W. R., Zhang, W., et al. (2019). Plasmaspheric hiss waves generate a reversed energy spectrum of radiation belt electrons. Nature Physics, 15(4), 367–372. https://doi.org/10.1038/s41567-018-0391-6

On the dynamics of ultra-relativistic electrons (>2 MeV) near L* = 3.5 during 8 June 2015

Authors: Benjamin Hogan[1,2], Xinlin Li[1,2], Zheng Xiang[3], Hong Zhao[4], Yang Mei[1,2], Declan O'Brien[1,2], Daniel N. Baker[1,2], Shrikanth Kanekal[5]

[1]Laboratory for Atmospheric and Space Physics, University of Colorado Boulder, Boulder, CO, USA. [2]Department of Aerospace Engineering Sciences, University of Colorado Boulder, Boulder, CO, USA. [3]Department of Space Physics, School of Electronic Information, Wuhan University, Wuhan, China. [4]Department of Physics, Auburn University, Auburn, AL, USA. [5]NASA Goddard Space Flight Center, Greenbelt, MD, USA.

Corresponding author: Benjamin Hogan (ben.hogan@lasp.colorado.edu)

Key points

1. A local minimum in >2 MeV electron phase space density is shown to form rapidly near L*=3.5 during a moderate storm of minimum Dst=-67 nT
2. EMIC wave characteristics are shown during this event, and we use quasi-linear theory to evaluate their role in this loss
3. Pitch-angle diffusion simulations with scattering rates due to O+ band EMIC waves are shown to reproduce the observed loss at L*=3.5

Abstract

Understanding local loss processes in Earth's radiation belts is critical to understanding their overall structure. Electromagnetic ion cyclotron waves can cause rapid loss of multi-MeV electrons in the radiation belts and contribute to an uncommon three-belt structure in the radiation belts. These loss effects have been observed at a range of L* values, recently as low as L* = 3.5. Here, we present a case study of an event where a local minimum develops in multi-MeV electron phase space density near L* = 3.5 and evaluate the possibility of EMIC waves in contributing to the observed loss feature. Signatures of EMIC waves are shown including rapid local loss and pitch angle bite outs. Analysis of the wave power spectral density during event shows EMIC wave occurrence at higher L* values. Using these representative wave parameters, we calculate minimum resonant energies, diffusion coefficients, and simulate the evolution of electron PSD during this event. From these results, we find that O+ band EMIC waves could be contributing to the local loss feature during this event. O+ band EMIC waves are uncommon, but do occur in these L* ranges, and therefore may be a significant driver of radiation belt dynamics under certain preconditioning of the radiation belts.

1. Introduction

Earth's radiation belts are normally a two-belt structure of energetic particles, with an inner belt which consists primarily of 100s of keV electrons and 10s to 100s of MeV protons with peak fluxes at L ≈ 2-3, and an outer belt of mainly 100s of keV to >MeV electrons with peak intensity near L = 4-5. L is the McIlwain L value, the distance in Earth radii (R_E) at which a dipole field line crosses the geomagnetic equatorial plane (McIlwain, 1961). The high energy electron populations in the outer belt exhibit various dynamics due to solar driving of the magnetosphere. The Van Allen Probes (formerly known as Radiation Belt Storm Probes, or RBSP) mission has provided valuable insight to the behavior of these energetic particles (Mauk et a., 2012). One of the early discoveries of the Van Allen Probes era was the identification of a third radiation belt, a storage ring of multi-MeV electrons near the inner edge of the outer radiation belt which is not generally observed (Baker et al., 2013). This was characterized by a reduction in flux of multi-MeV electrons in the region $3.5 < L^* < 4.0$ resulting in local peaks in fluxes in the region $3.0 < L^* < 3.5$ and at $L^* > 4.0$. L^* is the Roederer L value and is inversely proportional to the third adiabatic invariant (Roederer 1970), and $L^* \approx L$ for the low values of interest discussed here, although their unit is different (Roederer and Lejosne, 2018, Xiang et al., 2017).

Various driving mechanisms in the inner magnetosphere cause dynamics of trapped particle populations. Here, we highlight effects most prevalent in the dynamics of these multi-MeV electrons in the radiation belts. Phase space density (PSD) is often used to visualize these mechanisms, which is related to particle flux divided by the square of the particle's momentum (e.g., Chen et al., 2006). Trapped particles will undergo radial diffusion, a process referred to as a random walk due to varying electric and magnetic fields around the Earth (e.g., Barker et al., 2005; Lesjone et al., 2020). Radial diffusion will cause particles to reduce local radial gradients that develop in PSD (e.g., Green & Kivelson, 2004). The Dst effect changes the drift orbit radius of trapped particles during geomagnetic storms, as drift shells increase in radius to conserve the third adiabatic invariant in response to the reduction in Earth's magnetic field strength, resulting in a measured reduction in flux at a fixed radial distance as particles move outward (Kim & Chan et al., 1997; Li et al., 1997). This process is an adiabatic process and PSD will reverse to pre-storm levels with the recovery of Dst. Magnetopause shadowing is another driver of dynamics which occurs during storms when the solar wind compresses Earth's magnetosphere inward and reduces the last closed drift shell (LCDS) (e.g., Turner et al., 2014, Xiang et al., 2018). Particles outside of the LCDS are lost and particles near the LCDS are then exposed to rapidly formed gradients in PSD due to the outward loss of particles. Earthward particles of the LCDS then radially diffuse outward toward the gradient near the magnetopause and can also be lost outward of Earth's magnetosphere.

Wave-particle interactions can also cause loss of radiation belt populations and are energy-dependent due to resonance conditions with the timescales of invariant motions of trapped particles. Chorus waves can cause precipitation of MeV electrons on timescales of several days (Orlova & Shprits, 2014). Chorus wave loss is generally observed outside of the plasmasphere, a region of dense cold plasma with a varying outer boundary generally confined to $L<4$ (e.g., Thorne 2010). Hiss waves are observed within the plasmasphere and can preferentially scatter several hundreds of keV electrons (e.g., Ni et al., 2019; Zhao et al., 2019). Hiss waves can also cause weak loss of MeV electrons on timescales of days to months (Malaspina et al., 2016; Selesnick et al., 2003; Thorne et al., 2013). Another type of wave which prominently affects MeV energy electrons are electromagnetic ion cyclotron (EMIC) waves (e.g., Summers et al., 2007). EMIC waves effects are observed as fast, local losses of multi-MeV electrons satisfying resonance conditions (e.g., Aseev et al., 2017; Drozdov et al., 2019, 2020, 2022; Shprits et al., 2016, 2017; Usanova et al., 2014; Xiang et al., 2017). Local extrema which form due to these loss processes can result in radiation belt features such as the third radiation belt. The three-belt structure first reported by Baker et al., (2013), with a storage ring of multi-MeV electrons found near the inner edge of the outer belt, is shown to be reproduced in simulation models only with the inclusion of EMIC wave effects (Shprits et al., 2016). Therefore, understanding the effects of EMIC waves on multi-MeV electron populations near the inner edge of the outer belt is critical to understanding the overall structure of the radiation belts. Their effects on multi-MeV electrons are characterized in recent studies using the rich data collected by the Van Allen Probes Relativistic Electron Proton Telescope (REPT) data, with notable features such as multi-MeV electron loss by up to 2 orders of magnitude within satellite passes, limiting electron lifetimes, and producing bite outs in the pitch angle spectra (Baker et al., 2021; Su et al., 2017). We present here a discussion of the EMIC wave loss mechanism.

EMIC waves pitch angle scatter electrons into the loss cone via doppler-shifted resonance with electrons (Thorne and Kennel, 1971). EMIC waves most easily scatter particles at low equatorial pitch angles already near the loss cone, and narrowing of the pitch angle spectra, or “bite-out” features in multi-MeV electron flux have been shown to accompany EMIC wave occurrences (e.g., Aseev et al., 2017; Usanova et al., 2014). However, these studies have not made efforts to numerically quantify the relationship between flux evolution due to EMIC waves and the development of these bite outs. To decrease the entire pitch angle spectra, other waves that have stronger effects at all pitch angles such as chorus and hiss waves are likely required in concert with EMIC waves to produce whole-spectra losses (Drozdov et al., 2020; Ross et al., 2021). EMIC waves can only affect electrons of above specific energies, described as the minimum resonant energy of the electrons (e.g., Summers & Thorne, 2003). The minimum resonant energy as a function of pitch angle is dependent upon the solution of the plasma dispersion relation describing the wave behavior in the local plasma environment. Local loss processes such as EMIC wave scattering are apparent in radial PSD profiles as rapid decay at a specific L* value where the EMIC waves are present which can induce local minimums.

However, variations in L* locations of EMIC wave effects on multi-MeV electrons are reported; for example, at L* = 4.0 (Shprits et al., 2017, 2022), at L* = 4.2 (Lyu et al., 2022), L*> 4.2, (Xiang et al., 2017), L* = 4.5 (Usanova et al., 2014), and at L* = 4.7 (Aseev et al., 2017) during various events. A study of Van Allen Probes and GOES observations by Drozdov et al., (2022) showed that local PSD minimums are most common for several-MeV electron populations in the range L* = 4-5. Furthermore, the PSD minimums reported by the study by Drozdov et al., (2022) were reproduced only with EMIC wave effects included in a simulation model. A study by Cervantes et al., (2020) of Van Allen Probes data from October 2012-2016 found that EMIC waves on average affect $\mu \geq 900$ MeV/G electrons in the range L* = 3.6 - 6 and are the dominant loss process during storms near the inward edge of multi-MeV electron loss observations. Clearly, variations exist in the spatial extent of EMIC wave induced PSD minimums of multi-MeV electrons. Furthermore, the inward location of these PSD features and their driving mechanisms must be understood due to their contributions of local minimums in multi-MeV electron populations which contributes to the formation of the three-radiation belt structure. Hogan et al., (2021) reported an energy-dependent local minimum in multi-MeV electron PSD that forms over a long-term period from March to June 2015 near L* = 3.5, lower than where EMIC wave-induced loss has been reported before with event studies. PSD minimums in this L* region can be difficult to find with automatic detection algorithms such as those used by Drozdov et al., (2022) due to low PSD at small L* values. The dwell time of the spacecraft also decreases at low L* value, making the occurrence of these features less likely to be reported (e.g., Chen et al., 2019, Saikin et al., 2015, Sigsbee et al., 2023).

Statistical studies of EMIC wave occurrence during the Van Allen Probes era describe the spatial occurrence and frequency of these waves. Saikin et al., (2015) compiled EMIC wave observations using Van Allen Probes data from 2012-2015 and Sigsbee et al., (2023) studied the same data set until June 2016. Both studies showed that most observations of H+ and He+ band EMIC waves occur between L = 4-6, and O+ band waves are mostly observed at L < 2-4. Chen et al., (2019) studied the Van Allen Probes data set until 31 December 2017 and reported H+, He+, and O+ band EMIC waves to occur primarily in the regions $5 \leq L \leq 6.5$, $3 \leq L \leq 4.5$, and $3 \leq L \leq 4$ for each species. The majority of EMIC events, regardless of wave band, occur in the region $5 \leq L \leq 6$, with 35% of EMIC waves observed are in the H+ band, 59% were He+ band, and 7% were O+ band waves (Saikin et al., 2015). Sigsbee et al., (2023) report EMIC waves are observed ~2.4% of the time during the Van Allen Probes era, considering data from both Probes. Studies by Yu et al., (2015) suggest that O+ band waves can grow strongly near the plasmapause boundary region where the oxygen torus forms (e.g., Nosé et al., 2015), thus their increased observational occurrence in the low L region.

This study analyzes a moderate storm on 8 June 2015 during which Hogan et al., (2021) reported the formation of a local minimum in PSD in March-June 2015 at L* = 3.5, lower than where EMIC wave-induced local minimums had been reported before and lower than where the more common H+ and He+ EMIC waves are generally observed. We investigate the physical mechanism responsible for this local minimum by analysis of multi-MeV electron measurements, wave observations by the spacecraft, and consideration of wave particle interaction theory for the local plasma environment. PSD and flux features shown during the event are consistent with prior observations and theory of multi-MeV electron interactions with EMIC waves. EMIC waves in the O+ band will be shown to be the most likely contributor of this minimum from analysis using wave-particle interaction theory. Analysis of the wave power spectral density during the event is conducted and calculation of minimum resonant energies and diffusion coefficients for representative EMIC waves during the event are found. These diffusion coefficients are then used in a one-dimensional pitch-angle diffusion simulation to model the effects of EMIC waves during the event of study, showing the feasibility of O+ band EMIC waves in contributing to the observed loss. We discuss these results and present conclusions for the reader.

2. Instrumentation and methods

2.1. Data

Data from the Van Allen Probes mission is utilized for this study (Mauk et al., 2012). The Van Allen Probes consisted of two nearly identical probes launched into near-identical following orbits on 30 August 2012 and provided near-continuous measurements of the radiation belts until 18 October 2019 (Probe A) and 19 July 2019 (Probe B). Various onboard instruments provided simultaneous measurements of particles and waves in the radiation belts. The Energetic Particle Composition and Thermal Plasma Suite (ECT) provided energetic particle measurements and included the Relativistic Electron Proton Telescope (REPT) instrument (Baker et al., 2012). REPT provides >MeV electron energy measurements with high count rates, even at low L values where fluxes are low, due to its large geometric factor (0.2 $cm^2 sr$). We use this electron flux data to calculate electron PSD (e.g., Chen et al., 2006). The ECT Magnetic Ephemeris files (MagEphem) are also utilized here, in which adiabatic coordinates have been computed for selected magnetic field model configurations. Here, we use calculated adiabatic coordinates found using the TS04D magnetic field model, which should account for storm-time differences in the magnetic field (Tsyganenko & Sitnov, 2005). Magnetometer data from the Electric and Magnetic Field Instrument Suite and Integrated Science (EMFISIS) (Kleitzing et al., 2013) is inspected using methods for analyzing a tri-axial magnetometer (Bortnick et al., 2009; Usanova et al., 2012). We also use data from EMFISIS for obtaining an estimate of the local number density of electrons from analysis of the observed upper-hybrid frequency, identification of the plasmapause boundary, and determining the local magnetic field strength.

2.2. Theory

Wave-particle interaction theory predicts the energy exchange behavior of a wave and a trapped particle's invariant motion. L-mode EMIC waves are expected to have doppler-shifted gyroresonance with electrons of given energies (Kennel and Thorne, 1971). This is true when the following resonance condition is satisfied:

$$\omega - kv_{||} = N|\Omega_e|/\gamma \qquad (1)$$

where ω is the frequency of the wave, k is the parallel wave number found from the plasma dispersion relation, N is the cyclotron resonance harmonic, Ω_e is the electron gyrofrequency, $\gamma = (1 - v^2/c^2)^{-1/2}$ is the Lorentz factor, $v = (v_{||}^2 + v_{\perp}^2)^{1/2}$ is the electron speed, and $v_{||}$ and $v_{\perp}$ are the velocity components parallel and perpendicular to the ambient magnetic field. The minimum energy of electrons E_{min} (in units of $m_e c^2$) that will have gyrofrequencies which satisfy resonance this resonance condition is:

$$E_{min} = \left[1 - (v_{||})^2/c^2\right]^{-1/2} - 1 \qquad (2)$$

where $v_{||}/c$ is the ratio of the particle's parallel velocity $v_{||}$ to the speed of light c, and $v_{||}$ is found via the solution of equation (1) which therefore depends on the solution of a plasma dispersion relation (e.g., Summers & Thorne 2003). Here, we assume a cold plasma dispersion relation as described by Summers & Thorne (2003) and Summers et al., (2007). The strength of pitch angle scattering by L-mode EMIC waves can also be quantified by quasi-linear interaction theory as described by the pitch angle diffusion coefficient $D_{\alpha\alpha}$. $D_{\alpha\alpha}$ as described by Summers et al., (2007) for these waves is:

$$D_{\alpha\alpha} = \frac{\pi}{2}\frac{1}{\rho}\Omega_e^2 \frac{1}{(E+1)^2}\sum_j \frac{R\left(1-\frac{x_j cos\alpha}{y_j\beta}\right)^2 |dx_j/dy_j|}{\delta x|\beta cos\alpha - dx_j/dy_j|} e^{-\left(\frac{x_j - x_m}{\delta x}\right)^2} \quad (3)$$

where ρ describes the Gaussian spectral density of the wave, Ω_e is the electron gyrofrequency, E is the dimensionless particle kinetic energy, $\beta = [E(E+2)]^{1/2}/(E+1)$, R is the ratio of the relative wave power, x_j and y_j are the wave frequencies and wave numbers which are the resonant roots for the wave found from the plasma dispersion relation, δx and x_m are also found from these roots, and j is the number of roots. See Summers et al., (2007) for a full discussion of this equation. The solution of the minimum resonant energy of an electron with an EMIC wave (equation 2) depends on the solution of a plasma dispersion relation, which is a function of the local ion composition, number density, and magnetic field. The diffusion coefficient (equation 3) also depends on these parameters, as well as the relative power of the wave to the background magnetic field, and the assumed Gaussian spectral density of the wave power.

To compute the minimum resonant energy and diffusion coefficients for EMIC waves of interest in this study we use the Full Diffusion Code (Ni et al., 2008, 2011; Shprits and Ni et al., 2009). This model calculates minimum resonant energies and diffusion coefficients for input wave parameters based on wave-particle interaction theory described above. With the modeled diffusion coefficients, a one-dimensional pure pitch-angle diffusion equation (e.g., Ni et al., 2015) is solved numerically to simulate the time-evolution of electron phase space density:

$$\frac{\partial f}{\partial t} = \frac{1}{T(\alpha_{eq})\sin(2\alpha_{eq})}\frac{\partial}{\partial \alpha_{eq}}\left[T(\alpha_{eq})\sin(2\alpha_{eq})\,\langle D_{\alpha\alpha}\rangle \frac{\partial f}{\partial \alpha_{eq}}\right] \quad (4)$$

where f is phase space density, t is time, α_{eq} is equatorial pitch angle, $\langle D_{\alpha\alpha}\rangle$ is the bounce-averaged pitch angle diffusion coefficient, and the normalized electron bounce period $T(\alpha_{eq}) = 1.3802 - 0.3198\left[sin(\alpha_{eq}) + \sqrt{sin(\alpha_{eq})}\right]$ (Lenchek et al., 1961).

3. 8 June 2015 Event Study

Hogan et al., (2021) reported daily-averaged PSD between 26 March – 20 June 2015 and showed the development of a local minimum in PSD near L* = 3.5. During this period the time of greatest deepening of the observed minimum was during a moderate geomagnetic storm on 8 June 2015, where the Dst_{min} reached -67 nT. Panel a of Figure 1 shows the Dst during this event and vertical-colored lines denote times where the satellite observes multi-MeV electrons at K = 0.10

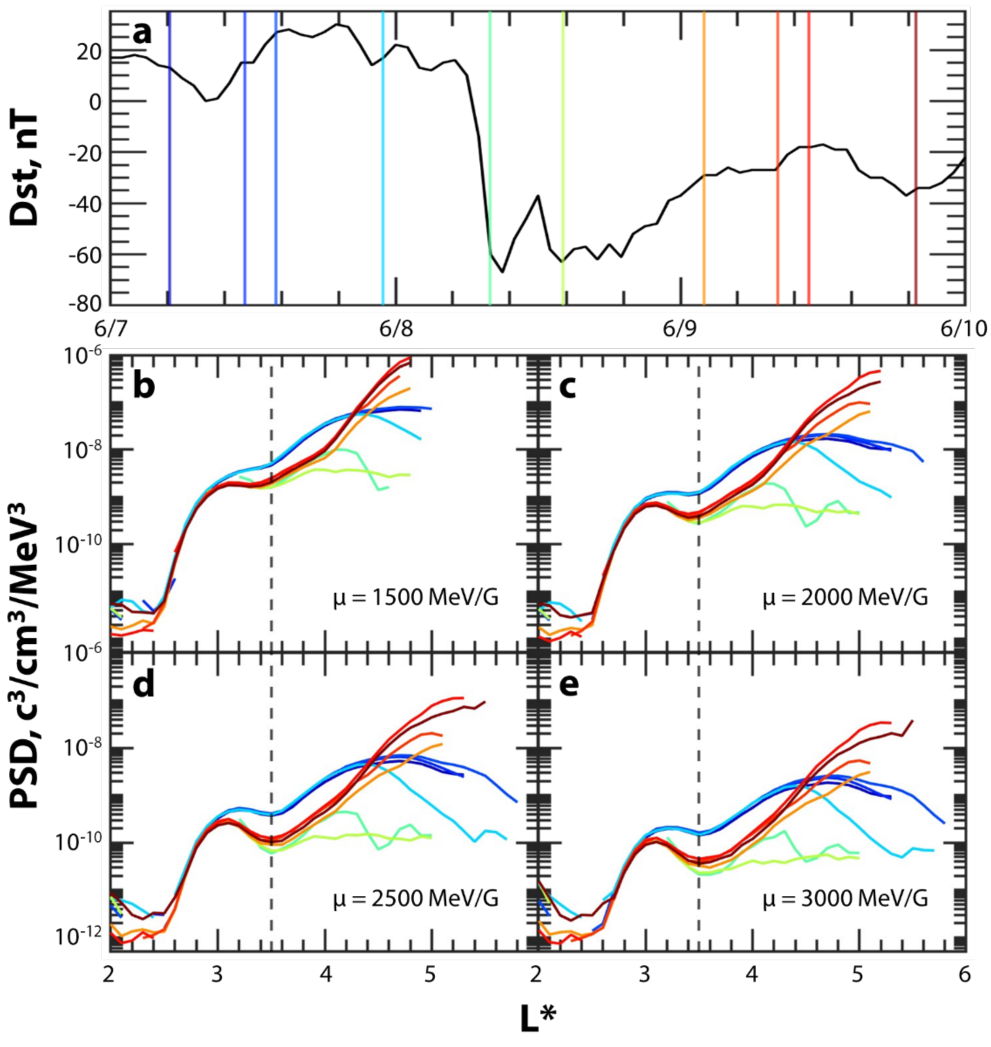

Figure 1. Panel A: Dst for 7-9 June 2015. Vertical lines indicate passes where Van Allen Probe A observes multi-MeV electrons at L* = 3.5, K = 0.10 $G^{1/2}R_E$. Panels b – e show pass averaged radial PSD profiles for K = 0.10 $G^{1/2}R_E$ and μ = 1500, 2000, 2500, and 3000 MeV/G respectively. The colors of the radial profiles correspond to the times shown for the same-colored lines in panel a. A vertical dashed line at L* = 3.5 is shown in panels b – e.

$G^{1/2}R_E$ and L* = 3.5 for 7 through 9 June 2015. These vertical lines are plotted at the center time of each of these observation bins from each satellite pass. Panels b through e show radial profiles of PSD during this period, averaged for each of these observation bins from satellite passes. The color of each profile corresponds to the passes indicated in panel a. PSD is calculated for diagnostic first adiabatic invariant values μ = 1500, 2000, 2500, and 3000 MeV/G, second adiabatic invariant value K = 0.10 $G^{1/2}R_E$, and L* bins ± 0.05. This value of K is selected as the lowest value at which multi-MeV electrons are nearly continuously observed by the Van Allen Probes mission. These narrow L* bins provide 21-28 data points per observation bin at L* = 3.5. The selected invariant values roughly correspond to 3.4, 4, 4.5, and 5.0 MeV electrons at L* = 3.5. Panel e shows that both inbound and outbound satellite passes of 3000 MeV/G electrons decrease by a factor of 6.8 within one satellite orbit near L* = 3.5 during this event, forming a local minimum in one satellite orbit. The loss is energy dependent, as seen by the increasing prominence of the minimum shown in panels B through D with increasing μ. Decreases by factors of 3.3, 4.5, 6.5, and 6.8 are shown for the 1500, 2000, 2500, 3000 MeV/G populations. Results here are shown from Van Allen Probe A. Results from Probe B for the same period are shown in the Supporting Information, and show the same local minimum at L* = 3.5 with similar decrease in one orbit, with a slight time shift due to the trailing Probe B passing the L* = 3.5 region ~one hour after Probe A. A comparison of PSD at L* = 3.5 from both spacecraft is also shown in the Supporting Information. We also note a slight variation in the precise L* location of the local minimum when found with fine L* bins 0.1 wide: at L* = 3.4, 3.5, and 3.5-3.6 for the 2000, 2500, and 3000 MeV/G electron populations. A local minimum also exists in PSD near L* = 4.5 during one satellite pass near the storm main phase, however this feature could be adiabatic as it does not exist in subsequent satellite passes, and perhaps is a function of the magnetic field model not accurately representing realistic L* values at high L* where the magnetic field can become more dynamic during the main phase of the storm.

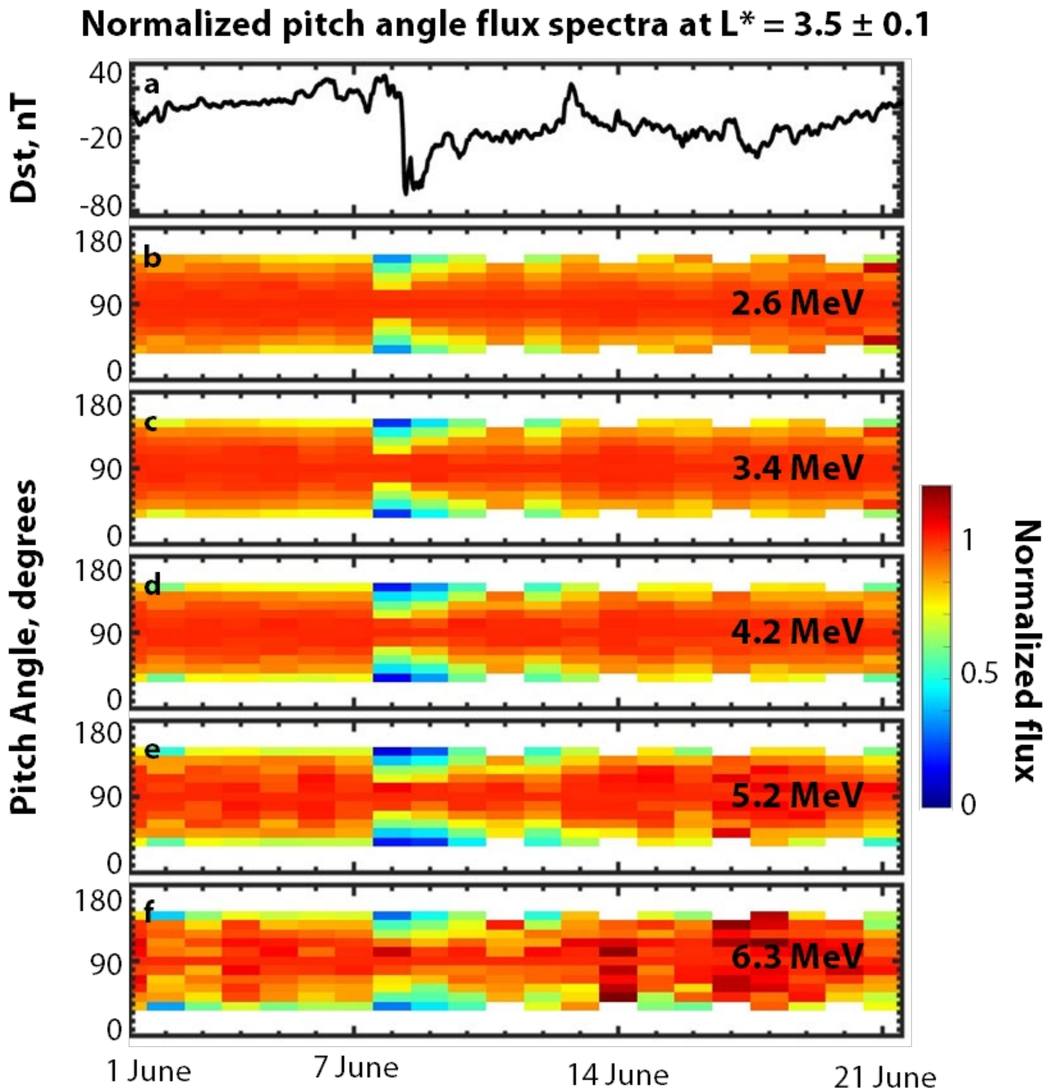

Figure 2 Dst, and daily-averaged normalized flux spectra from the 2.6 – 6.3 MeV energy channels from REPT for 1 – 21 June 2015. Data is from Van Allen Probe A. Normalized flux spectra are found by normalizing the pitch angle flux spectra to the 90-degree flux measurements.

Figure 2 shows the Dst in panel a and normalized flux spectra in panels b through f for the first three weeks of June 2015. The daily-averaged local flux spectra at L* = 3.5 are normalized in pitch angle to the 90-degree flux measurements to show the representative shape of the spectra (as in Aseev et al., 2017; Usanova et al., 2014). These measurements show that the pitch angle distribution of multi-MeV electrons is a common broad pancake distribution (e.g., Roederer 1970) in the pre-storm conditions of the event. On 8 June 2015 we show the presence of narrowing of the normalized-pitch angle spectra via strong losses in the normalized spectra at low-pitch angles relative to near-90° trapped particles, referred to as pitch angle bite outs (e.g., Bingley et al., 2019; Usanova et al., 2014). The pitch angle spectra then recover after the event to a broad pancake spectrum by 13 June for the remainder of the period shown. These bite-outs are shown in energies up to the 6.3 MeV energy channel measurements from REPT.

The wave power spectral density during 0 – 6 UT 8 June 2015 is shown in Figure 3 and is analyzed for signatures of EMIC waves. He+ and O+ gyrofrequencies are plotted and labeled in purple and are calculated using the magnitude of the measured magnetic field at the spacecraft. The H+ gyrofrequency is greater than those shown here, however, no relevant features are present in the wave power spectral density at these higher frequencies, therefore we focus on features in wave power at <5 Hz in Figure 3. We note the regions of contamination in these measurements in Figure 3. The constant power through the ion gyrofrequencies and constant vertical bands of wave power spectral density near 1:30-2:30 UT is likely instrument contamination as wave power will generally exhibit cutoffs near the gyrofrequencies due to the dampening effects of the actual ion-electron interactions (e.g., Fraser, 1985). Analysis is also conducted to find wave normal angle and ellipticity. These calculated parameters from the magnetometer data are analyzed for signatures of EMIC waves: wave power one order of magnitude greater than the average power in a frequency bin over the time range of study, wave normal angles <30 degrees, and ellipticity close to -1

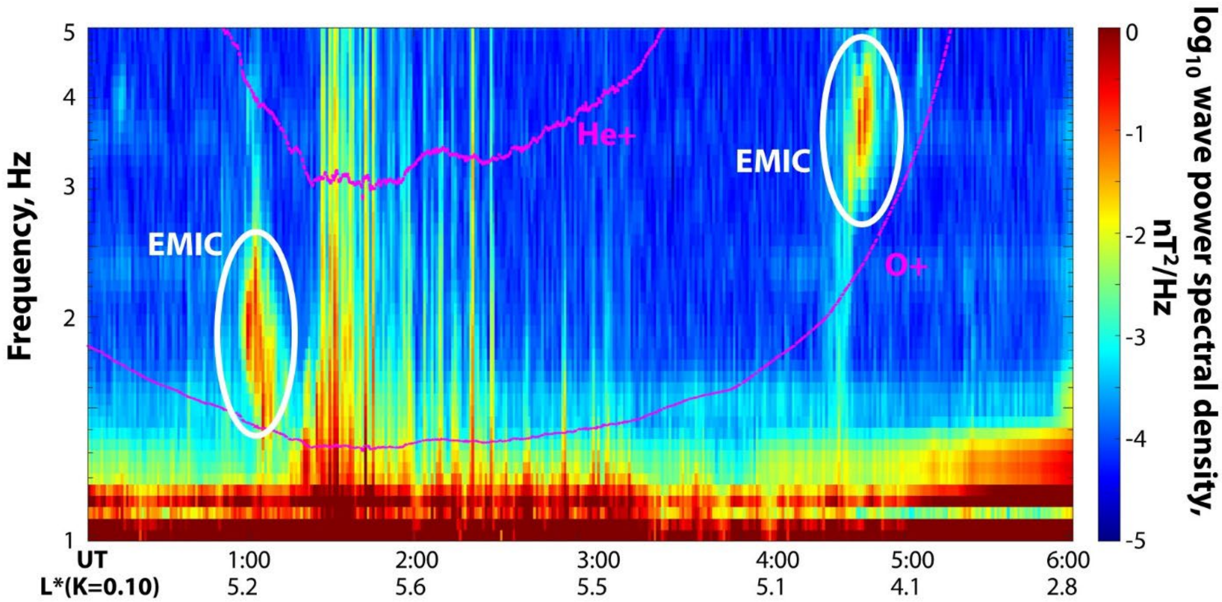

Figure 3 Wave power spectral density for 0-6 UT 8 June 2015. Data is from Van Allen Probe A. He+ and O+ ion gyrofrequencies are plotted in purple using the measured magnetic field from the EMFISIS instrument. Regions of EMIC power are identified and labeled. L* values corresponding to K = 0.10 $G^{1/2}R_E$ at each hour are reported below the x-axis.

indicating left hand polarized waves, matching EMIC wave theory and results from statistical studies of EMIC wave observations (Cao et al., 2020; Chen et al., 2019; Saikin et al., 2015). Regions in which these criteria for EMIC waves are satisfied are circled in Figure 3. Near 1:00 UT and 4:45 UT there are signatures of EMIC waves shown in the He+ band just above the O+ frequency, characteristic of where bursts of wave power are commonly observed relative to the local ion gyrofrequencies (e.g., Usanova et al., 2021). We note here this observation of EMIC waves occurs near L* = 4.2 – 4.3, higher than where the observation of rapid loss is shown near L* = 3.5. Similar analysis from RBSP B does not show any EMIC wave signatures during 7-8 June 2015.

The results in Figure 1 indicate a loss process that is energy dependent with loss which increases with μ and occurs on timescales within one 9-hour satellite orbit. The results in Figure 2 show accompanying pitch angle bite outs with these observations. The local number density is also analyzed as found from EMFISIS data and indicates local number density ~960 cm^{-3} at L* = 3.5 during the satellite pass of interest, indicating that the satellite is in a region of dense plasma and likely within the plasmapause, normally indicated by number densities >100 cm^{-3}. Local number density has also been used to identify the plasmapause crossings during the Van Allen Probes era by the EMFISIS data team. These results show that the spacecraft is within the plasmasphere during this loss event. The local number density and plasmapause crossing locations found from the local number density are shown in the Supporting Information. Plasmapause crossings of L* = 4.6 are indicated in the orbit preceding the observed loss, and compression of the plasmapause to L* = 3.9 is indicated during the pass where rapid PSD loss is first observed. Thus, the observed feature at L* = 3.5 occurs well within the plasmapause boundary. Chorus waves do not propagate well within the dense plasmapause (e.g., Meredith et al., 2001). Hiss waves can occur within the plasmapause but have not been shown to strongly affect MeV electrons on these timescales (e.g., Malaspina et al., 2016; Selesnick et al., 2003; Thorne et al., 2013). Rather, hiss waves preferentially affect 100s of keV electrons (e.g., Ni et al., 2019; Zhao et a., 2019), much lower than the >MeV populations affected here. Therefore, neither chorus nor hiss wave-particle interactions are likely to a prominent driver of multi-MeV electron dynamics during this event at L* = 3.5. PSD increases at higher L* values, suggesting no readily apparent effects of magnetopause shadowing on the trapped particle populations at L* = 3.5. The loss feature is shown to persist in pass-averaged PSD through the ~2-day period after the initial loss observation shown, and the resulting local minimum in PSD exists until a strong storm on 21-23 June 2015 in daily-averaged PSD (Hogan et al., 2021). The persistence of this feature with Dst recovery indicates that the process is not adiabatic and the Dst effect is not causing these dynamics. Furthermore, radial diffusion should oppose the formation of PSD gradients and local extrema such as reported here, thus the process occurring exceeds the effects of radial diffusion. EMIC waves are the most likely driving mechanism as their effects are strong within the plasmapause, preferentially affect electrons of increasing energies (specifically in the >MeV range), cause loss on rapid timescales, are shown to cause rapid-forming pitch angle bite outs and are shown to contribute to the formation of similar minimums in PSD at higher-L* values. EMIC waves are also observed during the satellite orbit where the rapid loss is shown, however at higher L* values. Therefore, due to the lack of likely contributions from other established drivers of multi-MeV electron loss, EMIC wave effects arise as the most likely mechanism to contribute to this PSD minimum at L* = 3.5. We here quantify the effects of EMIC waves on the PSD population observed using wave-particle interaction theory.

4. PSD simulations and comparisons with observations

We calculate minimum resonant energies and diffusion coefficients from EMIC waves using quasi-linear theory to estimate the timescale of loss due to these waves. These values are found using the full diffusion code (Ni et al., 2008, 2011; Shprits and Ni et al., 2009) which solves equations (2), (3), and the solution of a cold plasma dispersion relation. Input parameters are derived from spacecraft measurements when possible. Electron number density is 960 cm^{-3} as derived from EMFISIS measurements. Wave shape is found from a Gaussian fit of the form $\exp(-[\mathrm{f}-\mathrm{f_m}]/\delta f)^2$ to the time-averaged power near 4:45 UT which fulfills EMIC wave criteria with the parameters $\mathrm{f_m}$ = 0.57 Hz and δf = 0.045 Hz (shown in the Supporting Information). The local equatorial magnetic field strength is found to be 647 nT from EMFSIS measurements. The local plasma composition is taken to be 70% H+, 20% He+, and 10% O+ as found by Meredith et al., (2003) and as used for similar diffusion coefficient calculations (e.g., Summers & Thorne, 2003; Usanova et al., 2014). The EMIC waves are assumed to be confined within ±15° as consistent with observations of other EMIC wave events (Chen et al., 2019, Saikin et al., 2015). The wave normal angle is assumed to have a quasi-parallel distribution (e.g., Ni et al., 2015). The effects of polarization reversal are not considered here (e.g., Cao et al., 2020). We here consider orders of cyclotron resonance from -5 to 5. The EMIC waves are assumed to be left-hand polarized as considered for prior EMIC wave diffusion coefficient theory (Summers et al., 2007) and as observed for EMIC waves observed at higher L* values during the event, shown in Figure 3. Two different cases are evaluated for the diffusion coefficients due to EMIC waves at L* = 3.5 in the absence of their direct observation, scaling the frequency of the nearby observed wave power to the time when the spacecraft crosses L* = 3.5 using the local magnetic field strength, or assuming similar waves as those observed at higher L* values. These two cases are presented in this study: First, we consider He+ band EMIC waves, which are the band in which EMIC wave power is observed during the satellite orbit of loss as shown in Figure 3. The frequency range of the wave spectrum is normalized to the time when the spacecraft passes L* = 3.5 based on measurements of the magnetic field strength during 04:38:40 – 04:49:56 UT. This normalization is done by scaling the central frequency of the wave and the wave power spectral width such that the ratio of these parameters to the He+ frequency band are the same as the observations of the nearby EMIC wave power. Second, we normalize the frequency range of the spectrum based on a magnetic field strength of 647 nT. This frequency range of the spectrum is located mainly in the O+ band when the spacecraft is in the region near L* = 3.5, thus the waves are treated as O+ band EMIC waves with an upper frequency limit of 0.99 times the local O+ gyrofrequency. This allows for the consideration and comparison of the effects of He+ and O+ band EMIC waves during the event with realistic wave parameters as observed during the satellite orbit of interest, as no EMIC waves are directly observed during the spacecraft crossing of L* = 3.5 during which the rapid PSD loss is observed.

The minimum resonant energies and pitch angle diffusion coefficients for each of these cases are shown in Figure 4. Minimum resonant energies are indicated by the minimum energy at which the diffusion coefficient is defined at a given pitch angle, the waves do not resonate with electrons at energies where the diffusion coefficient is not defined. The value of the pitch angle diffusion coefficient is indicated by the color scale in Figure 4. The calculated energy and cross diffusion terms are multiple orders of magnitude less than the calculated pitch angle diffusion coefficients; we will focus only on the effects of pitch angle diffusion here. The dispersion relationship results, explicit resonant regions, and energy and cross diffusion terms are shown in the Supporting Information. Panel A shows the results for He+ band EMIC waves, and that they do not resonate with electrons less than 56 MeV at $\alpha_{eq} = 54°$ (which corresponds to K = 0.10

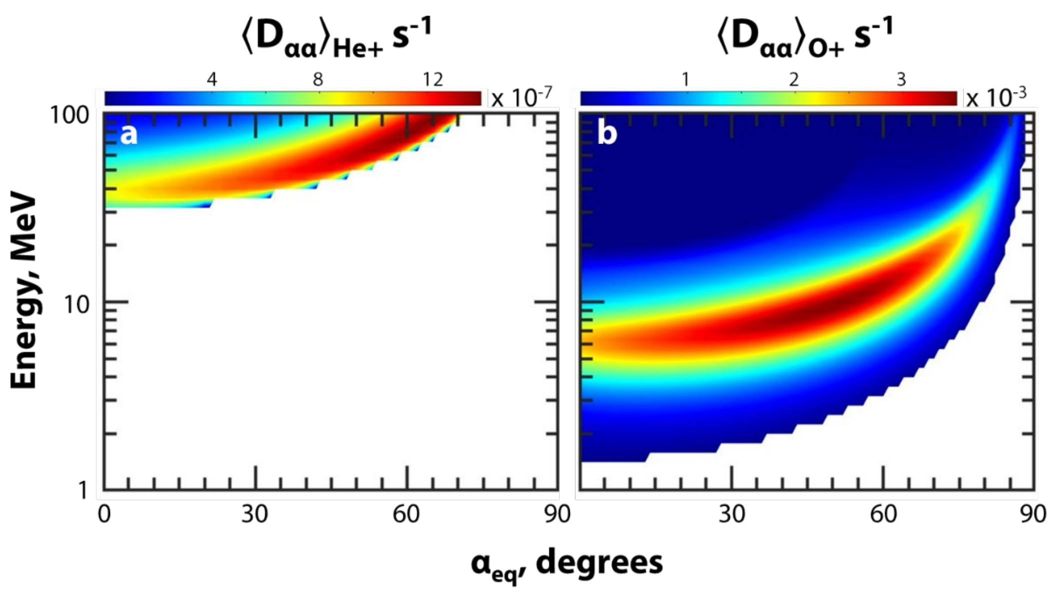

Figure 4 Panel a: minimum resonant energy and bounce-averaged diffusion coefficient calculated for He+ band EMIC waves with the described input parameters. Minimum resonant energies are the lowest energy at each pitch angle for which the diffusion coefficient is defined. The strength of the diffusion coefficient is indicated by the color bar on top of the plot. Panel b: Same as left, but for O+ band EMIC waves.

$G^{1/2}R_E$ at L* = 3.5 during this event), much higher than the energies where loss is observe. In panel b, we show that representative O+ band EMIC waves can resonate with electrons down to 2.8 MeV energies at $\alpha_{eq} = 54°$, encompassing the electron energies observed to decrease during this event of study. The diffusion coefficients due to O+ band waves are also much larger – about 4 orders of magnitude greater when comparing peak values in the energy ranges presented here. We also show in Figure 4 that the diffusion coefficient increases with increasing electron energy from ~MeV to several MeV, which matches the behavior of the loss mechanism observed and shown in Figure 1.

To model the effects of these diffusion coefficients on electron PSD we use a one-dimensional pitch angle diffusion model (equation 4) (e.g., Ni et al., 2015). Boundary conditions for modeled PSD f are $df/dt(\alpha_{eq} = 90°) = 0$ and $f(\alpha_{eq} < \alpha_{loss\ cone}) = 0$. The first condition is an upper boundary condition stating that there should not be any change in PSD for particles that are perfectly trapped, and the second condition defines that PSD within the loss cone should exhibit rapid loss during the simulation. We assume the initial PSD profile follows a sine function in equatorial pitch angle (e.g., Ni et al., 2013, 2015). We match the prescription of initial PSD to the PSD observations from RBSP A shown in Figure 1, noting that the observations shown in Figure 1 are for second adiabatic invariant K = 0.10 $G^{1/2}R_E$ which corresponds to $\alpha_{eq} = 54°$ at L* = 3.5 during this event. PSD evolution is simulated by solving equation (1) over one 9-hour satellite orbit and shown in Figure 5 for the 3000 MeV/G population, which corresponds to ~5 MeV electrons at L* = 3.5 and K = 0.10 $G^{1/2}R_E$. We assume EMIC waves are present for 2% of

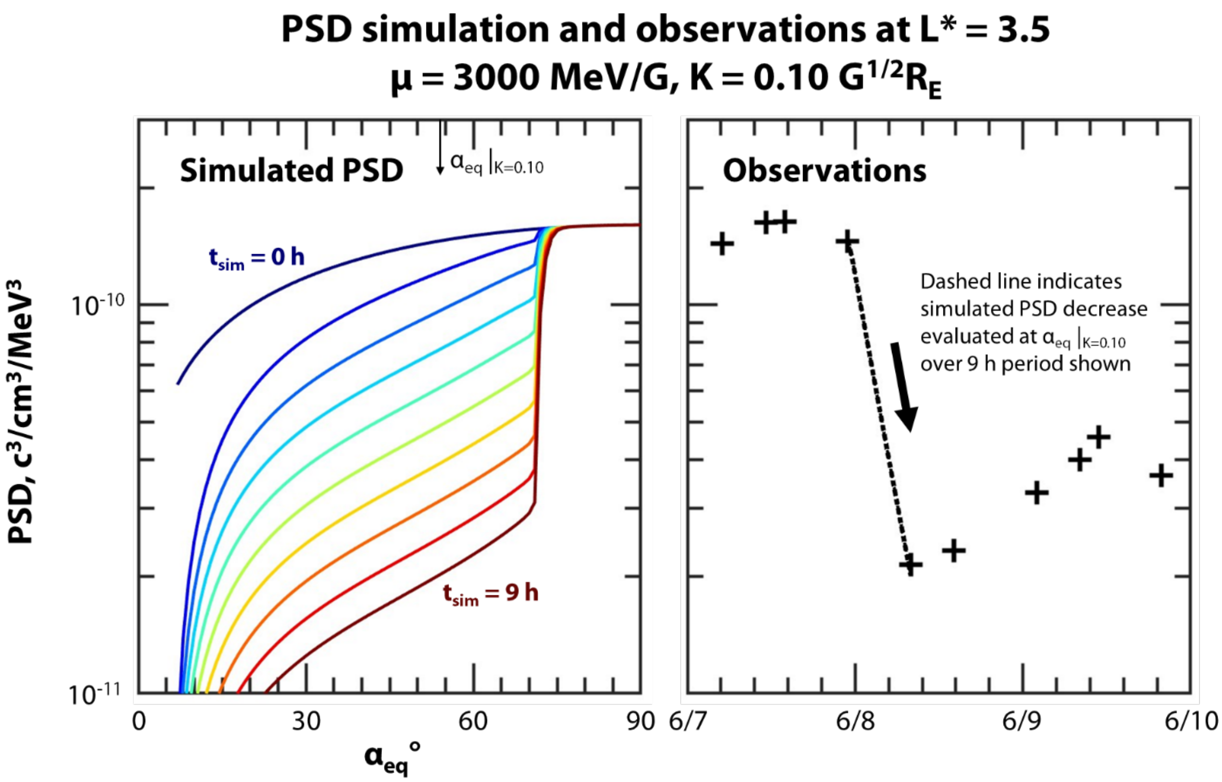

Figure 5 Left: simulated PSD for μ = 3000 MeV/G, K = 0.10 $G^{1/2}R_E$ electrons using the pure pitch angle diffusion model described in the text. The pitch angle corresponding to K = 0.10 $G^{1/2}R_E$ is indicated on the top x-axis, and the initial PSD value at this pitch angle is prescribed to match the observed PSD by Van Allen Probe A immediately before the observed loss at L* = 3.5. The evolution of PSD is plotted every hour and progresses from blue to red for 9-hours. Right: Pass-averaged PSD from Van Allen Probe A for μ = 3000 MeV/G, K = 0.10 $G^{1/2}R_E$ electrons at L* = 3.5 plotted with + marks for 7 through 9 June 2015. Simulated PSD (shown on the left) is evaluated at the pitch angle corresponding to K = 0.10 $G^{1/2}R_E$ and shown with a dashed line, starting from the satellite pass point used for initial conditions for the PSD simulation.

the drift orbit of the electrons, similar to MLT drift orbit averaging assumed by other studies (e.g., Summers et al., 2007) and agreeing with the occurrence rate ranges of O+ band EMIC waves at L* = 3.5 (Chen et al., 2019; Saikin et al., 2015). These simulation results are shown in the left panel of Figure 5. The initial spectrum of PSD is shown in blue, for we prescribe such that the PSD at $\alpha_{eq} = 54°$ agrees with the observations from Van Allen Probe A from the pass immediately before the rapid decrease in PSD. We plot PSD spectra progression every hour with color progressing from red to blue. Results in Figure 5 are for μ = 3000 MeV/G electrons over 9-hours, which is one satellite orbit, the amount of time during which Van Allen Probe A observes rapid PSD loss. This simulation result in Figure 5 shows the significant and fast decrease in PSD at $\alpha_{eq} \lesssim 70°$, and the narrowing of the pitch angle spectra over the course of the satellite orbit simulated. In the right panel of Figure 5, we compare this simulation result (dashed line) with the observed PSD from Van Allen Probe A from 7 through 9 June 2015. Observed PSD at L* = 3.5, K = 0.10 $G^{1/2}R_E$ is shown for each satellite pass and indicated by + marks. Evaluating the simulation result at $\alpha_{eq} = 54°$, we show here good agreement between the simulated PSD loss due to EMIC wave effects and the observations, under the simulation conditions and diffusion coefficients found as described.

Results shown in Figure 5 are for 3000 MeV/G electrons and show a decrease by a factor of 7.2, compared to observational decrease of 6.8 over a 9-hour period. Similar analysis is done for the 1500, 2000, and 2500 MeV/G populations, for which we report respective decreases by factors of 2.8, (3.2 observed), 3.6 (4.5 observed), 5.0, (6.5 observed), 7.2 (6.8 observed) for these populations over the 9-hour period. These results for all μ values are shown in the Supporting Information.

5. Discussion

The calculation of diffusion coefficients for representative EMIC waves during the event as shown in Figure 4 indicates that EMIC waves in the O+ band and not the He+ band can be driving the loss of electrons at multi-MeV energies as shown in Figure 1. We modeled PSD evolution using these EMIC wave effects and pure pitch angle diffusion. The results in Figure 5 show decrease of PSD at lower pitch angles while preserving the populations at higher pitch angles, thus narrowing the pitch angle spectra, as observed during the event and shown in Figure 5. O+

band EMIC waves are less common than He+ band EMIC waves as found by studies of EMIC observations from the Van Allen Probes era (Sigsbee et al., 2023, Chen et al., 2019, Yu et al., 2015); however, when O+ EMIC waves are observed, they are most prevalent in the range $3 < L < 4$, which is the region where this loss is observed, and are as common as H+ EMIC waves in this region (Chen et al., 2019; Saikin et al., 2015). The dwell time of the spacecraft decreases with L value (as shown by Chen et al., 2019; Sigsbee et al., 2023; Yu et al., 2015) decreasing the likelihood of observing EMIC wave structures in this region. Studies by Yu et al., (2015) of the early Van Allen Probes era (2012-2014) suggest that O+ EMIC waves are found generally in the outer plasmasphere and occasionally the plasma trough which is the region in which this loss process is observed. In this region the O+ density can be higher than the partial ion compositions used here, thus increasing the strength of O+ band EMIC waves. A study of Van Allen Probes data from 2012-2017 by Chen et al., (2019) shows that O+ band waves do occur mostly in the region 3-3.5 R_E, which corresponds to this region of loss. This study also showed that O+ band EMIC waves are observed to have small wave normal angles and linear polarization as assumed here. EMIC waves can be bursty and occur on short timescales making them difficult to be fully measured in time and space even by a two-spacecraft mission, but EMIC effects can be observed in these multi-MeV electrons which have drift periods on the timescale of minutes and transport information about the waves to the satellite for measurement. O+ band waves specifically are thought to happen near the plasmapause boundary where the oxygen torus (e.g., Nose et al., 2015) expands and leads to growth of O+ band waves in this region (Yu et al., 2015). During the event of study, no appreciable O+ density increase was shown using partial ion densities as found from the Helium, Oxygen, Proton, and Electron (HOPE) instrument, or from inferred ion densities down to >eV energies using the methods of Goldstein et al., (2013), as shown in the Supporting Information. Therefore, it is not clear that the oxygen torus is present during this event.

Minimum resonant energies and the strength of diffusion coefficients from EMIC wave effects will vary due to the temperature of the ions and the local ion composition, as seen in equations (1) and (2). Here, we have assumed a cold plasma, and the solution of a cold plasma dispersion relation is used for computing the results of equations (1) and (2) as developed by Summers & Thorne (2003) and Summers et al., (2007). Sensitivity of the solutions of plasma dispersion relations when using cold, warm, or hot plasma dispersion relations have been discussed in previous studies, and have been shown to affect the solution by changing the wave number solution which changes the resonant conditions (e.g., Bashir et al., 2021, 2022; Lee et al., 2014). However, these observations and modeling in this study are made at low L* values where the local number density is near 1000 cm^{-3} and within the plasmapause. Therefore, a cold plasma approximation is an accurate assumption for the solutions of (1) and (2). Similar use of the cold plasma dispersion relation has been used for calculating diffusion coefficients for EMIC waves up to L* = 4.5 (Usanova et al., 2014).

Ion compositions must also be assumed due to the lack of direct in-situ measurements. In certain events when EMIC waves are observed in multiple bands, one can estimate the local ion compositions (e.g., Min et al., 2015; Qin et al., 2019). However, in the event of study, only one band is shown, and at higher L* values than where the observed loss feature occurs. Therefore, the local ion composition must be assumed. The solution of the plasma dispersion relation is sensitive to the local ion composition (e.g., Bashir et al., 2021, 2022; Summers et al., 2007). The assumed compositions found by Meredith et al., (2003) however provide adequate representative parameters for the local ion compositions and have been used for similar studies of diffusion coefficients from EMIC waves (e.g., Usanova et al., 2014). Furthermore, the minimum resonant energy does not vary as strongly with ion composition as it does with other parameters (such as local number density, which is inferred from satellite measurements during the event). Significant deviation from statistically found average EMIC wave characteristics and ion compositions would be required for He+ band waves to affect the populations where loss is observed, therefore it is more likely here that O+ band waves are affecting these multi-MeV electrons at L* = 3.5 than He+ band waves.

Here we have only modeled the effects of L-mode quasi-linear EMIC waves. Other studies acknowledge that often the combined effects of EMIC waves with other waves such as chorus or hiss waves chorus and/or hiss waves are required to produce loss of the entire pitch angle spectra to fully match observations of loss at high α_{eq} (Drozdov et al., 2020; Qin et al., 2019; Ross et al., 2021). We show here that EMIC wave effects can account for the loss in PSD shown and can induce narrowing of the pitch angle spectra, but that other loss mechanisms must be present to affect the dynamics of higher pitch angle electrons, PSD at high pitch angles remain constant in our simulations as shown in Figure 5 due to the lack of a defined pitch angle diffusion coefficient at that region for the electron populations of study. Hiss waves are prevalent within the plasmapause can scatter particles to the pitch angles where they can then be affected by EMIC waves (e.g., Drozdov et al., 2020; Li et al., 2007). The loss feature at L* = 3.5 is shown to be within the plasmapause here as shown here. A study of multi-MeV electron flux data from the Van Allen Probes in 2015 by Ross et al., (2021) suggested that hiss wave and EMIC waves are both required to reproduce observed loss at L* ≤ 3.75. While their study did not include O+ band EMIC waves due to their low occurrence rate, we show here that representative O+ band waves alone can account for large loss in multi-MeV electron PSD on rapid timescales during the event of study.

Other governing factors of the simulation space may be found to affect the L* dependence of local minimums in PSD. Preconditioning of the system may be important for these structures, as EMIC wave effects are generally most prevalent when the wave first interacts with the dense plasmasphere (e.g., Usanova et al., 2021). Compression of the plasmapause may be necessary for EMIC wave effects to cause local minimums in multi-MeV electrons at lower L* values, such as during the strong storm in March 2015 before this observation (Dst_{min} = -234). During the period after the March 2015 storm through June 2015, Hogan et al., (2021) show the development of the local minimum at L* = 3.5 discussed here. During this period and before the 8 June event studied in detail here, other moderate storms in terms of Dst are present: 10-11 April (Dst_{min} = -85 nT), 15-19 April (Dst_{min} = -88 nT), and 11-13 May (Dst_{min} = -82 nT). Decay of PSD at L* = 3.5 during these events contributes to local loss but not the formation of a local minimum in PSD, only during the 8 June event is the PSD low enough at L* = 3.5 that a minimum can then form. Loss during these events prior moderate events may have been preferential at L* = 3.5 as well, and perhaps governed by the same mechanisms as those discussed here, as EMIC waves are most effective at causing loss when first crossing the plasmapause, regardless of wave band. While continuous O+ band waves are unlikely due to their infrequent observations, it is possible that EMIC waves in the He+ or H+ bands are causing local loss during these prior storms, or other mechanisms not revealed in this event study are present. Hiss waves also affect multi-MeV electrons on these multi-month timescales and may play a part in the preconditioning of PSD at L* = 3.5 for the 8 June 2015 event as well. This topic warrants future research as the loss at certain L* values can lead to the formation of the third radiation belt and significantly affect dynamics of the radiation belt structure, and here, driving mechanisms of uncommon wave types (O+ band EMIC waves) are shown to be able to be capable of causing this feature during only a moderate geomagnetic storm in terms of Dst (Dst_{min} = -67 nT) under the given preconditioning. Therefore, future study is required.

6. Conclusions

1. Rapid loss of multi-MeV electron PSD is shown during a moderate storm with minimum Dst = -67 nT. This loss is primarily at L* = 3.5 and causes a local PSD minimum to form within one satellite orbit. The loss is shown to be energy dependent, with increasing prominence of the local minimum with increasing μ.
2. Pitch angle bite outs are shown in multi-MeV electron flux channels from the REPT instrument during this event, indicating narrowing of the pitch angle distribution and a loss mechanism that affects multi-MeV electrons most strongly at lower pitch angles.
3. Quasi-linear theory is used to analyze the effects of He+ and O+ band waves for the plasma environment at L* = 3.5 during the event. Analysis of minimum resonant energies due to each wave type show O+ band waves as a possible driver of multi-MeV electron dynamics. Representative O+ band EMIC wave effects are simulated in a one-dimensional pitch angle diffusion model of PSD using initial conditions observed during the event and calculated diffusion coefficients. These simulation results show that O+ band EMIC waves can produce loss rates similar to the observed multi-MeV PSD loss at L* = 3.5 in one satellite orbit.

Acknowledgements

REPT data and RBSP Magnetic Ephemeris data are provided by the Energetic Particle, Composition, and Thermal Plasma Suite (ECT) (Spence et al., 2013). We thank the REPT team (Baker et al., 2012) as well as the EMFISIS team (Kletzing et al., 2013) for use of their respective instrument data. ECT data used in this study is available from https://rbsp-ect.newmexicoconsortium.org/data_pub/. EMFISIS data are is available from the NASA OMNI web database: https://omniweb.gsfc.nasa.gov/. Plasmapause location determined from local number density measurements by Craig Kletzing is available at https://emfisis.physics.uiowa.edu/Events/rbsp-a/plasmapause/. Dst values are provided by Kyoto University: wdc.kugi.kyoto-u.ac.jp. The authors thank Alexander Drozdov and Mary Hudson for valuable discussions regarding this work. This work has been supported in part by NSF grant AGS 1834971, NASA grants NSSC19K0237, 80NSSC20K0913, and 80NSSC21K0583. NASA/RBSP-ECT funding is from JHU/APL contract 967399 under prime NASA contract NAS5-01072. H. Zhao is supported by NSF grant AGS 2140933, 2131012, 2247857, and NASA grant 80NSSC22K0473.

References

Aseev, N. A., et al. “Signatures of Ultrarelativistic Electron Loss in the Heart of the Outer Radiation Belt Measured by Van Allen Probes.” *Journal of Geophysical Research: Space Physics*, vol. 122, no. 10, 2017, https://doi.org/10.1002/2017ja024485.

Bashir, M. F., Artemyev, A., Zhang, X.-J., & Angelopoulos, V. (2022). Energetic electron precipitation driven by the combined effect of ULF, EMIC, and whistler waves. Journal of Geophysical Research: Space Physics, 127, e2021JA029871. https://doi.org/10.1029/2021JA029871

Bashir, M. F., Artemyev, A., Zhang, X.-J., & Angelopoulos, V. (2022). Hot plasma effects on electron resonant scattering by electromagnetic ion cyclotron waves. Geophysical Research Letters, 49, e2022GL099229. https://doi. org/10.1029/2022GL099229

Baker, D. N., et al. “The Relativistic Electron-Proton Telescope (REPT) Instrument on Board the Radiation Belt Storm Probes (RBSP) Spacecraft: Characterization of Earth’s Radiation Belt High-Energy Particle Populations.” *Space Science Reviews*, vol. 179, no. 1-4, 2012, pp. 337–381., https://doi.org/10.1007/s11214-012-9950-9.

Baker DN, Kanekal SG, Hoxie VC, Henderson MG, Li X, Spence HE, Elkington SR, Friedel RH, Goldstein J, Hudson MK, Reeves GD, Thorne RM, Kletzing CA, Claudepierre SG. A long-lived relativistic electron storage ring embedded in Earth's outer Van Allen belt. Science. 2013 Apr 12;340(6129):186-90. doi: 10.1126/science.1233518. Epub 2013 Feb 28. PMID: 23450000.

Barker, A. B., Li, X., & Selesnick, R. (2005). Modeling the radiation belt electrons with radial diffusion driven by the solar wind. Space Weather, 3, S10003. https://doi.org/10.1029/2004SW000118

Bingley, L., Angelopoulos, V., Sibeck, D., Zhang, X., Halford, A. The evolution of a pitch-angle “bite-out” scattering signature caused by EMIC wave activity: a case study. J. Geophys. Res. Space Phys. 124, 5042–5055 (2019). https://doi.org/10.1029/2018JA026292

Bortnik, J., et al. “An Automatic Wave Detection Algorithm Applied to PC1 Pulsations.” *Journal of Geophysical Research: Space Physics*, vol. 112, no. A4, 2007, https://doi.org/10.1029/2006ja011900.

Cao, Xing, et al. “Effects of Polarization Reversal on the Pitch Angle Scattering of Radiation Belt Electrons and Ring Current Protons by Emic Waves.” *Geophysical Research Letters*, vol. 47, no. 17, 2020, https://doi.org/10.1029/2020gl089718.

Cervantes, S., et al. “Quantifying the Effects of Emic Wave Scattering and Magnetopause Shadowing in the Outer Electron Radiation Belt by Means of Data Assimilation.” Journal of Geophysical Research: Space Physics, vol. 125, no. 8, 2020, https://doi.org/10.1029/2020ja028208.

Chen, Y., et al. “Phase Space Density Distributions of Energetic Electrons in the Outer Radiation Belt during Two Geospace Environment Modeling Inner Magnetosphere/Storms Selected Storms.” *Journal of Geophysical Research*, vol. 111, no. A11, 2006, https://doi.org/10.1029/2006ja011703.

Chen, H., Gao, X., Lu, Q., & Wang, S. (2019). Analyzing EMIC waves in the inner magnetosphere using long-term Van Allen Probes observations. Journal of Geophysical Research: Space Physics, 124, 7402–7412. https://doi.org/ 10.1029/2019JA026965

Drozdov, A. Y., Aseev, N., Effenberger, F., Turner, D. L., Saikin, A., & Shprits, Y. (2019). Storm time depletions of multi-MeV radiation belt electrons observed at different pitch angles. Journal of Geophysical Research: Space Physics, 124, https://doi.org/10.1029/2019JA027332

Drozdov, A. Y., et al. "Depletions of Multi-Mev Electrons and Their Association to Minima in Phase Space Density." Geophysical Research Letters, vol. 49, no. 8, 2022, https://doi.org/10.1029/2021gl097620.

Drozdov, A. Y., et al. "The Role of Hiss, Chorus, and Emic Waves in the Modeling of the Dynamics of the Multi-MeV Radiation Belt Electrons." (2020) Journal of Geophysical Research: Space Physics, vol. 125, no. 9, 2020, https://doi.org/10.1029/2020ja028282.

Fraser, B.J. Observations of ion cyclotron waves near synchronous orbit and on the ground. Space Sci Rev 42, 357–374 (1985). https://doi.org/10.1007/BF00214993

Goldstein, J., De Pascuale, S., Kletzing, C., Kurth, W., Erickson, P. J., Foster, J. C., Genestreti, K., Skoug, R. M., Larsen, B. A., Kistler, L. M., Mouikis, C., & Spence, H. (2014). Simulation of Van Allen Probes plasmapause encounters. Journal of Geophysical Research: Space Physics, 119, 7464– 484. https://doi.org/10.1002/2014JA020252

Green, Janet C and Kivelson. "Relativistic Electrons in the Outer Radiation Belt: Differentiating between Acceleration Mechanisms." *Journal of Geophysical Research*, vol. 109, no. A3, 2004, https://doi.org/10.1029/2003ja010153.

Hogan, Benjamin, et al. "Multi-MeV Electron Dynamics near the Inner Edge of the Outer Radiation Belt." *Geophysical Research Letters*, vol. 48, no. 23, 2021, https://doi.org/10.1029/2021gl095455.

Thorne, R. M., & Kennel, C. F. (1971). Relativistic electron precipitation during magnetic storm main phase. Journal of Geophysical Research, 76(19), 4446–4453. https://doi.org/10.1029/JA076i019p04446

Kim, H. J., & Chan, A. A. (1997). Fully adiabatic changes in storm time relativistic electron fluxes. Journal of Geophysical Research: Space Physics, 102(A10), 22107–22116. https://doi.org/10.1029/97ja01814

Kletzing, C. A., et al. "The Electric and Magnetic Field Instrument Suite and Integrated Science (EMFISIS) on RBSP." *Space Science Reviews*, vol. 179, no. 1-4, 2013, pp. 127–181., https://doi.org/10.1007/s11214-013-9993-6.

Lee, J. H., and Angelopoulos, V. (2014), Observations and modeling of EMIC wave properties in the presence of multiple ion species as function of magnetic local time, J. Geophys. Res. Space Physics, 119, 8942– 8970, doi:10.1002/2014JA020469.

Lenchek, A., S. Singer, and R. Wentworth (1961), Geomagnetically trapped electrons from cosmic ray albedo neutrons, J. Geophys. Res., 66(12), 4027–4046, doi:10.1029/JZ066i012p04027.

Lejosne, S., and Kollmann, P. (2020), Radiation Belt Diffusion at Earth and Beyond. *Space Science Reviews*. https://doi.org/10.1007/s11214-020-0642-6

Li, W., Shprits, Y. Y., & Thorne, R. M. (2007). Dynamic evolution of energetic outer zone electrons due to wave-particle interactions during storms. Journal of Geophysical Research, 112, A10220. https://doi.org/10.1029/2007JA012368

Li, X., Baker, D. N., Temerin, M., Cayton, T. E., Reeves, E. G. D., Christensen, R. A., et al. (1997). Multisatellite observations of the outer zone electron variation during the November 3–4, 1993, magnetic storm. Journal of Geophysical Research: Space Physics, 102(A7), 14123–14140. https://doi.org/10.1029/97ja01101

Li, W., & Hudson, M. K. (2019). Earth's Van Allen radiation belts: From discovery to the Van Allen Probes era. *Journal of Geophysical Research: Space Physics*, 124, 8319– 8351. https://doi.org/10.1029/2018JA025940
Malaspina, D. M., Jaynes, A. N., Boulé, C., Bortnik, J., Thaller, S. A., Ergun, R. E., & Wygant, J. R. (2016). The distribution of plasmaspheric hiss wave power with respect to plasmapause location. Geophysical Review Letters, 43, 7878–7886. https://doi.org/10.1002/2016GL069982
Mauk, B. H., et al. "Science Objectives and Rationale for the Radiation Belt Storm Probes Mission." (2012) *Space Science Reviews*, vol. 179, no. 1-4, 2012, pp. 3–27., https://doi.org/10.1007/s11214-012-9908-y.
Meredith, N. P., Horne, R. B., & Anderson, R. R. (2001). Substorm dependence of chorus amplitudes: Implications for the acceleration of electrons to relativistic energies. Journal of Geophysical Research, 106, 13165– 13178. https://doi.org/10.1029/2000JA900156
Meredith, Nigel P. "Statistical Analysis of Relativistic Electron Energies for Cyclotron Resonance with Emic Waves Observed on CRRES." *Journal of Geophysical Research*, vol. 108, no. A6, 2003, https://doi.org/10.1029/2002ja009700.
Min, K., Liu, K., Bonnell, J., Breneman, A., Denton, R., Funsten, H., et al. (2015). Study of EMIC wave excitation using direct ionmeasurements.Journal of Geophysical Research: Space Physics,120, 2702–2719
McIlwain, C. E. (1961). Coordinates for mapping the distribution of magnetically trapped particles. Journal of Geophysical Research, 66(11), 3681–3691. https://doi.org/10.1029/jz066i011p03681
Ni, B., R. M. Thorne, Y. Y. Shprits, and J. Bortnik (2008), Resonant scattering of plasma sheet electrons by whistler-mode chorus: Contribution to diffuse auroral precipitation, Geophys. Res. Lett., 35, L11106, doi:10.1029/2008GL034032.
Ni, B., R. M. Thorne, N. P. Meredith, R. B. Horne, and Y. Y. Shprits (2011), Resonant scattering of plasma sheet electrons leading to diffuse auroral precipitation: 2. Evaluation for whistler mode chorus waves, J. Geophys. Res., 116, A04219, doi:10.1029/2010JA016233.
Ni, B., J. Bortnik, R. M. Thorne, Q. Ma, and L. Chen (2013), Resonant scattering and resultant pitch angle evolution of relativistic electrons by plasmaspheric hiss, J. Geophys. Res. Space Physics, 118, 7740–7751, doi:10.1002/2013JA019260.
Ni, B., et al. (2015), Resonant scattering of outer zone relativistic electrons by multiband EMIC waves and resultant electron loss time scales, J. Geophys. Res. Space Physics, 120, 7357–7373, doi:10.1002/2015JA021466
Ni, B., Huang, H., Zhang, W., Gu, X., Zhao, H., Li, X., et al. (2019). Parametric sensitivity of the formation of reversed electron energy spectrum caused by plasmaspheric hiss. Geophysical Research Letters, 46(8), 4134–4143. https://doi.org/10.1029/2019gl082032
Nosé, M., Oimatsu, S., Keika, K., Kletzing, C. A., Kurth, W. S., De Pascuale, S., et al. (2015). Formation of the oxygen torus in the inner magnetosphere: Van Allen Probes observations. Journal of Geophysical Research: Space Physics, 120(2), 1182–1196. https://doi.org/10.1002/2014JA020593
Orlova K., Y. Shprits, (2014), Model of lifetimes of the outer radiation belt electrons in a realistic magnetic field using realistic chorus wave parameters, J. Geophys. Res. [Space Physics], 119, 770-780, doi:10.1002/2013JA019596
Qin, M., Hudson, M. K., Li, Z., Millan, R. M., Shen, X.-C., Shprits, Y. Y., et al. (2019). Investigating loss of relativistic electrons associated with EMIC waves at low L values on

22 June 2015. Journal of Geophysical Research: Space Physics, 124, 4022–4036. https://doi. org/10.1029/2018JA025726

Roederer, J. G. "Dynamics of Geomagnetically Trapped Radiation." *Physics and Chemistry in Space*, 1970, https://doi.org/10.1007/978-3-642-49300-3.

Roederer, J. G., & Lejosne, S. (2018). Coordinates for representing radiation belt particle flux. Journal of Geophysical Research: Space Physics,123, 1381- 1387. https://doi.org/10.1002/2017JA025053

Ross, J. P. J., Glauert, S. A., Horne, R. B., Watt, C. E. J., & Meredith, N. P. (2021). On the variability of EMIC waves and the consequences for the relativistic electron radiation belt population. Journal of Geophysical Research: Space Physics, 126, e2021JA029754. https://doi. org/10.1029/2021JA029754

Saikin, A. A., et al. "The Occurrence and Wave Properties of H + -, He + -, and O + -Band Emic Waves Observed by the Van Allen Probes." *Journal of Geophysical Research: Space Physics*, vol. 120, no. 9, 2015, pp. 7477–7492., https://doi.org/10.1002/2015ja021358.

Selesnick, R. S. "Atmospheric Losses of Radiation Belt Electrons." *Journal of Geophysical Research*, vol. 108, no. A12, 2003, https://doi.org/10.1029/2003ja010160.

Shprits, Y. Y., and B. Ni (2009), Dependence of the quasi-linear scattering rates on the wave normal distribution of chorus waves, J. Geophys. Res., 114, A11205, doi:10.1029/2009JA014223.

Shprits et al., 2016, Wave-induced loss of ultra-relativistic electrons in the Van Allen radiation belts, DOI: 10.1038/ncomms12883

Shprits, Y. Y., A. Kellerman, N. Aseev, A. Y. Drozdov, and I. Michaelis (2017), Multi-MeV electron loss in the heart of the radiation belts, Geophys. Res. Lett., 44, 1204–1209, doi:10.1002/ 2016GL072258.Schulz, Michael, and Louis J. Lanzerotti. "Particle Diffusion in the Radiation Belts." *Physics and Chemistry in Space*, 1974, https://doi.org/10.1007/978-3-642-65675-0.

Sigsbee, K., Kletzing, C. A., Faden, J., & Smith, C. W. (2023). Occurrence rates of electromagnetic ion cyclotron (EMIC) waves with rising tones in the Van Allen Probes data set. Journal of Geophysical Research: Space Physics, 128, e2022JA030548. https://doi. org/10.1029/2022JA030548

Spence, H. E., Reeves, G. D., Baker, D. N., Blake, J. B., Bolton, M., Bourdarie, S., et al. (2013). Science goals and overview of the radiation belt storm probes (RBSP) energetic particle, composition, and thermal plasma (ECT) suite on NASA's van allen Probes mission. Space Science Reviews, 179(1), 311–336. https://doi.org/10.1007/s11214-013-0007-5Summers & Thorne, (2003), Relativistic electron pitch-angle scattering by electromagnetic ion cyclotron waves during geomagnetic storms. Journal of Geophysical Research, Vol 108, N. A4, 1143, doi:10.1029/2002JA009489

Thorne, R. M., and Kennel, C.F (1971). Relativistic electron precipitation during magnetic storm main phase. Journal of Geophysical Research, Vol 76, Issue 19, 4446-4453. https://doi.org/10.1029/JA076i019p04446

Thorne, R. M. (2010). Radiation belt dynamics: The importance of wave-particle interactions. Geophysical Research Letters, 37, L22107. https://doi.org/10.1029/2010GL044990

R.M. Thorne, W. Li, B. Ni, Q. Ma, J. Bortnik, D.N. Baker, H.E. Spence, G.D. Reeves, M.G. Henderson, C.A. Kletzing, W.S. Kurth, G.B. Hospodarsky, D. Turner, V. Angelopoulos, Evolution and slow decay of an unusual narrow ring of relativistic electrons near L $\sim$ 3.2

following the September 2012 magnetic storm. Geophys. Res. Lett. 40(1-5), 3507–3511 (2013a). https://doi.org/10.1002/grl.50627

Tsyganenko, N. A., & Sitnov, M. I. (2005). Modeling the dynamics of the inner magnetosphere during strong geomagnetic storms. *Journal of Geophysical Research*, **110**, A03208. https://doi.org/10.1029/2004JA010798

Turner, D. L., Angelopoulos, V., Morley, S. K., Henderson, M. G., Reeves, G. D., Li, W., et al. (2014). On the cause and extent of outer radiation belt losses during the 30 September 2012 dropout event. Journal of Geophysical Research: Space Physics, 119(3), 1530–1540. https://doi. org/10.1002/2013ja019446

Su, Z., Gao, Z., Zheng, H., Wang, Y., Wang, S., Spence, H.E., Reeves, G.D., Baker, D.N., Wygant, J.R., Rapid loss of radiation belt relativistic electrons by EMIC waves. J. Geophys. Res. Space Phys. 122, 10 (2017). https://doi.org/10.1002/2017ja024169

Summers, D., and R. M. Thorne, Relativistic electron pitch-angle scattering by electromagnetic ion cyclotron waves during geomagnetic storms, J. Geophys. Res.,108(A4), 1143, doi:10.1029/2002JA009489, 2003

Summers, D., B. Ni, and N. P. Meredith (2007), Timescales for radiation belt electron acceleration and loss due to resonant wave-particle interactions: 1. Theory, J. Geophys. Res., 112, A04206, doi:10.1029/2006JA011801.

Usanova, M. E., I. R. Mann, J. Bortnik, L. Shao, and V. Angelopoulos (2012), THEMIS observations of electromagneticion cyclotron wave occurrence: Dependence on AE, SYMH, and solar wind dynamic pressure, J. Geophys. Res.,117, A10218, doi:10.1029/2012JA018049

Usanova, M. E., et al. "Effect of Emic Waves on Relativistic and Ultrarelativistic Electron Populations: Ground-Based and Van Allen Probes Observations." *Geophysical Research Letters*, vol. 41, no. 5, 2014, pp. 1375–1381., https://doi.org/10.1002/2013gl059024.

Usanova ME (2021) Energy Exchange Between Electromagnetic Ion Cyclotron (EMIC) Waves and Thermal Plasma: From Theory to Observations. Front. Astron. Space Sci. 8:744344. doi: 10.3389/fspas.2021.744344

Xiang, Zheng, et al. "Understanding the Mechanisms of Radiation Belt Dropouts Observed by Van Allen Probes." *Journal of Geophysical Research: Space Physics*, vol. 122, no. 10, 2017, pp. 9858–9879., https://doi.org/10.1002/2017ja024487.

Xiang, Z., Tu, W., Ni, B., Henderson, M. G., & Cao, X. (2018). A statistical survey of radiation belt dropouts observed by Van Allen Probes. Geophysical Research Letters, 45, 8035–8043. https://doi.org/ 10.1029/2018GL078907

Yu, X., Z. Yuan, D. Wang, H. Li, S. Huang, Z. Wang, Q. Zheng, M. Zhou, C. A. Kletzing, and J. R. Wygant (2015), In situ observations of EMIC waves in O+ band by the Van Allen Probe A, Geophys. Res. Lett., 42, 1312–1317, doi:10.1002/ 2015GL063250.

Zhao, H., Ni, B., Li, X., Baker, D. N., Johnston, W. R., Zhang, W., et al. (2019). Plasmaspheric hiss waves generate a reversed energy spectrum of radiation belt electrons. Nature Physics, 15(4), 367–372. https://doi.org/10.1038/s41567-018-0391-6

Journal of Geophysical Research: Space Physics

Supporting Information for

On the dynamics of ultra-relativistic electrons (>2 MeV) near L* = 3.5 during 8 June 2015

Benjamin Hogan[1,2], Xinlin Li[1,2], Zheng Xiang[3], Hong Zhao[4], Yang Mei[1,2], Declan O'Brien[1,2], Daniel N. Baker[1,2], Shrikanth Kanekal[5]

[1]Laboratory for Atmospheric and Space Physics, University of Colorado Boulder, Boulder, CO, USA, [2]Department of Aerospace Engineering Sciences, University of Colorado Boulder, Boulder, CO, USA, [3]Department of Space Physics, School of Electronic Information, Wuhan University, Wuhan, China [4]Department of Physics, Auburn University, Auburn, AL, USA, [5]NASA Goddard Space Flight Center, Greenbelt, MD, USA

Corresponding author: Benjamin Hogan (ben.hogan@lasp.colorado.edu).

Contents of this file

Figure S1: 7-9 June 2015 phase space density profiles from Van Allen Probe B

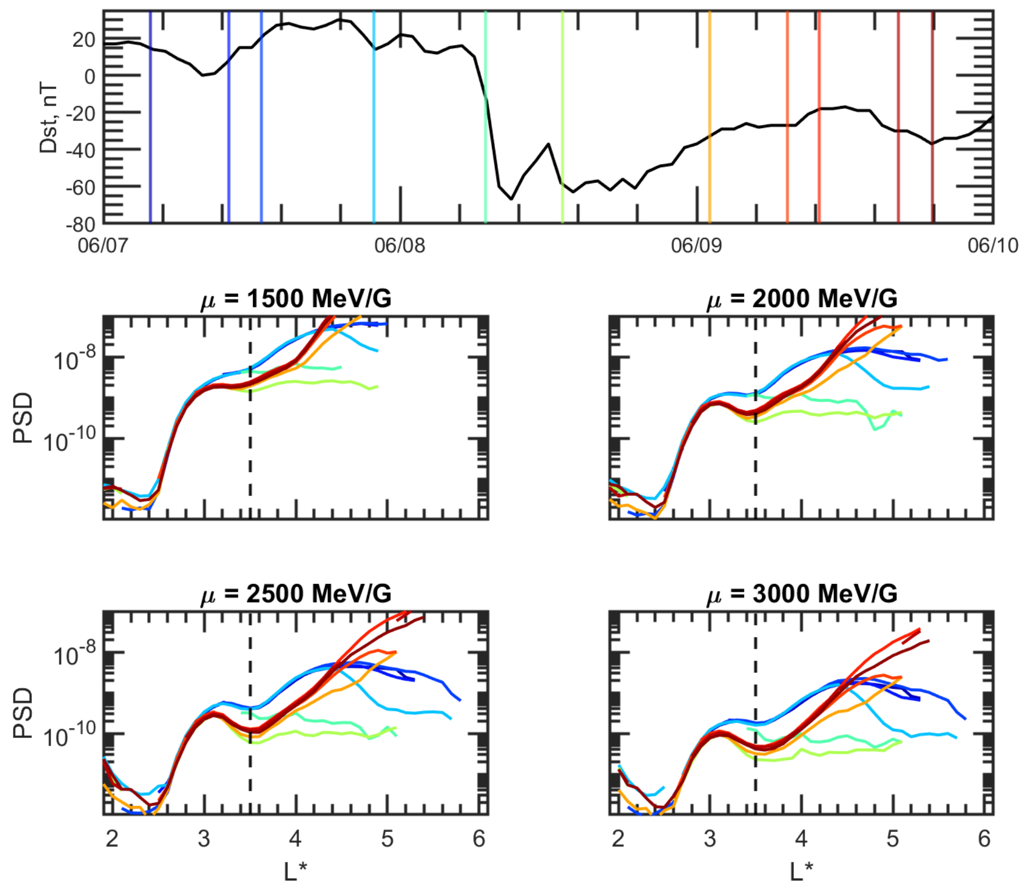

We focus on results from Van Allen Probe A data in the main text. Here, we present radial profiles of phase space density (PSD) for the same adiabatic invariant values and period as shown in Figure 1 of the main text, however, for Probe B. K = 0.10 $G^{1/2}R_E$ and L* bins are 0.1 wide, and adiabatic coordinates are found as calculated using the TS04D magnetic field model, as in Figure 1. We note that similar observations are made from the Probe B data, a local minimum that develops near L* = 3.5 for multi-MeV electron PSD. We note that Probe A observed during one satellite pass near the storm main phase a local extremum at L* = 4.5 that we proposed is an adiabatic effect and function of the local magnetic field not being accurately represented at high L* during the main phase of the storm. This effect is not shown here in the Probe B data, which substantiates that claim. Probe B makes one satellite observation of L* = 3.5, K = 0.10 $G^{1/2}R_E$ just as the decrease in Dst occurs. Therefore, the magnetic field model is also unlikely to perfectly represent the actual magnetic configuration during this time, which may contribute to the transitional measurement made by Probe B here during the satellite pass at ~6 UT 8 June 2015 which is denoted by a green line. The PSD profile at this time shows an intermediate measurement between the pre-storm PSD and the post-storm local minimum that develops at L* = 3.5.

Figure S2: 7-9 June 2015 phase space density at L* = 3.5 from both Probes

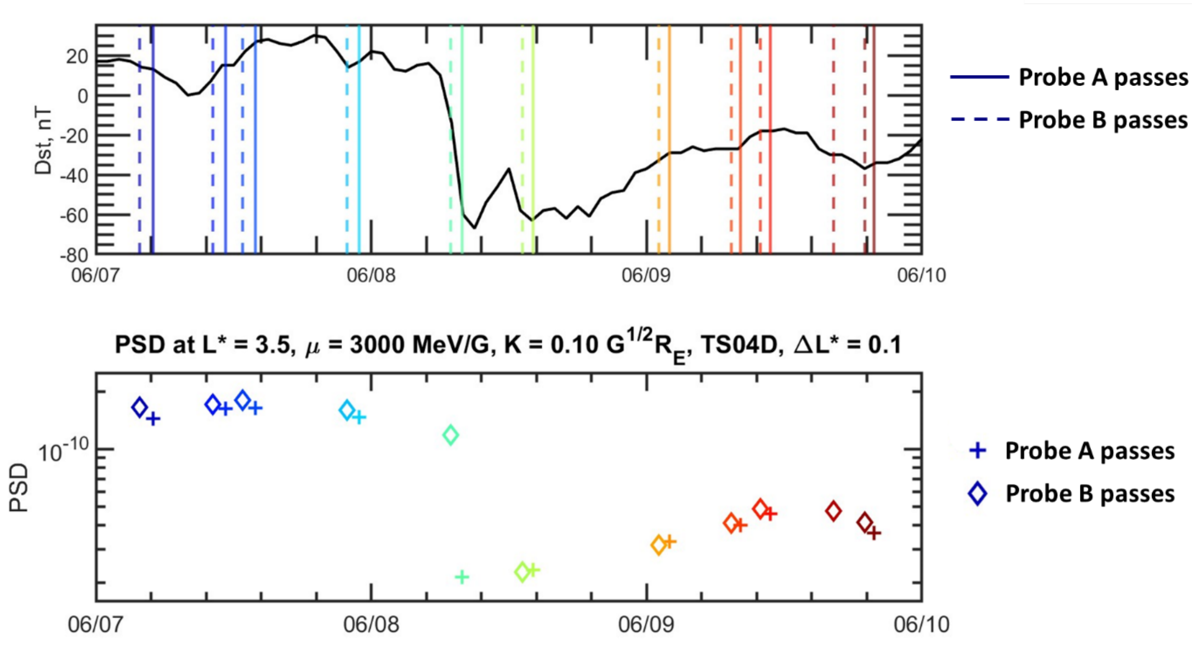

To compare the PSD specifically at L* = 3.5 during the event, and to compare the observations from Probe A and B, we show the PSD from each Probe at L* = 3.5 in Figure S2. The top panel shows the Dst for 7 through 9 June 2015, and vertical colored lines indicate passes by each Probe which observe multi-MeV electrons at L* = 3.5, K = 0.10 $G^{1/2}R_E$. Solid vertical lines indicate passes by Probe A, dashed vertical lines indicate passes by Probe B. In the bottom panel is the calculated PSD at μ = 3000 MeV/G, the highest energy population shown in the main text for which the local minimum in PSD develops. Diamonds indicate PSD calculated from Probe A measurements, and + marks indicate those from Probe B. Here we see the rapid decrease in PSD as seen by both Probes in the first half of 8 June 2015. However, Probe B maintains higher measurement of PSD for one more satellite pass than Probe A. The passes where Probe B maintains higher measurement near 6 UT 8 June 2015 and Probe A subsequently shows large decrease are indicated in green and are near the main phase of the storm. It is possible that during this rapid decrease in PSD, the magnetic field model is not accurately representing the real dynamics of Earth's magnetic field during this time, and that is contributing to a large perceived difference in the measurements from Probe A and B, which here occur within 1.1 hours. It is unlikely that the loss observed will occur within this 1.1-hour period alone, but possible over one satellite orbit. In subsequent data from the second half of 8 June 2015 and on, both Probes have similar PSD measurements.

Figure S3: Local number density and plasmapause crossings during 7-8 June 2015

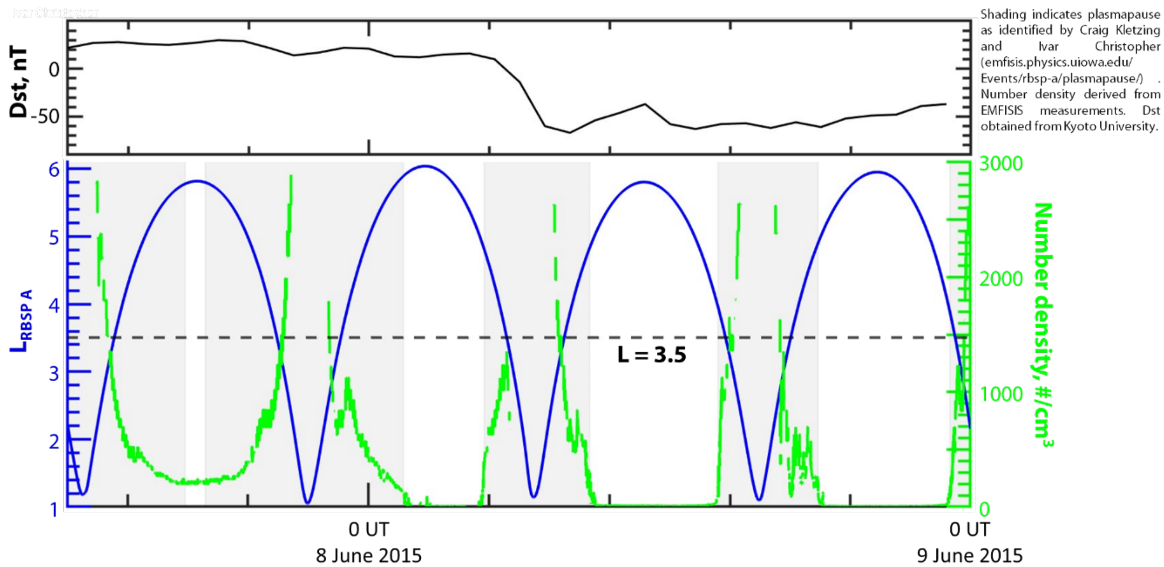

The local number density is important in this study as it affects the solution of the plasma dispersion relation and indicates which density region the spacecraft is in, relative to the plasmapause. In Figure S3 we show the Dst, and the number density as derived from EMFISIS data, and L value of the spacecraft for 12 UT 7 June – 0 UT 9 June 2015. Analysis of the local number density by EMFISIS PI Craig Kletzing has been conducted and the plasmapause crossings by the spacecraft are reported using this data. Using this information, we here shade regions where the spacecraft is within the plasmapause. A dashed horizontal line is shown at L = 3.5, near the region of PSD loss discussed in the manuscript. This shows that this region L = 3.5 is well within the plasmapause. Further inspection of the actual number density, shown in green on the right y axis, indicates local number density near and greater than ~1000 /cm^3, which indicates a dense and likely cold plasma region. Therefore, the observed loss feature occurs within the plasmapause, and a cold plasma dispersion relation as approximated in the manuscript is appropriate for modeling waves in the local medium.

Figure S4: Time-averaged wave power spectral density near 4:45 UT 8 June 2015 and Gaussian fit

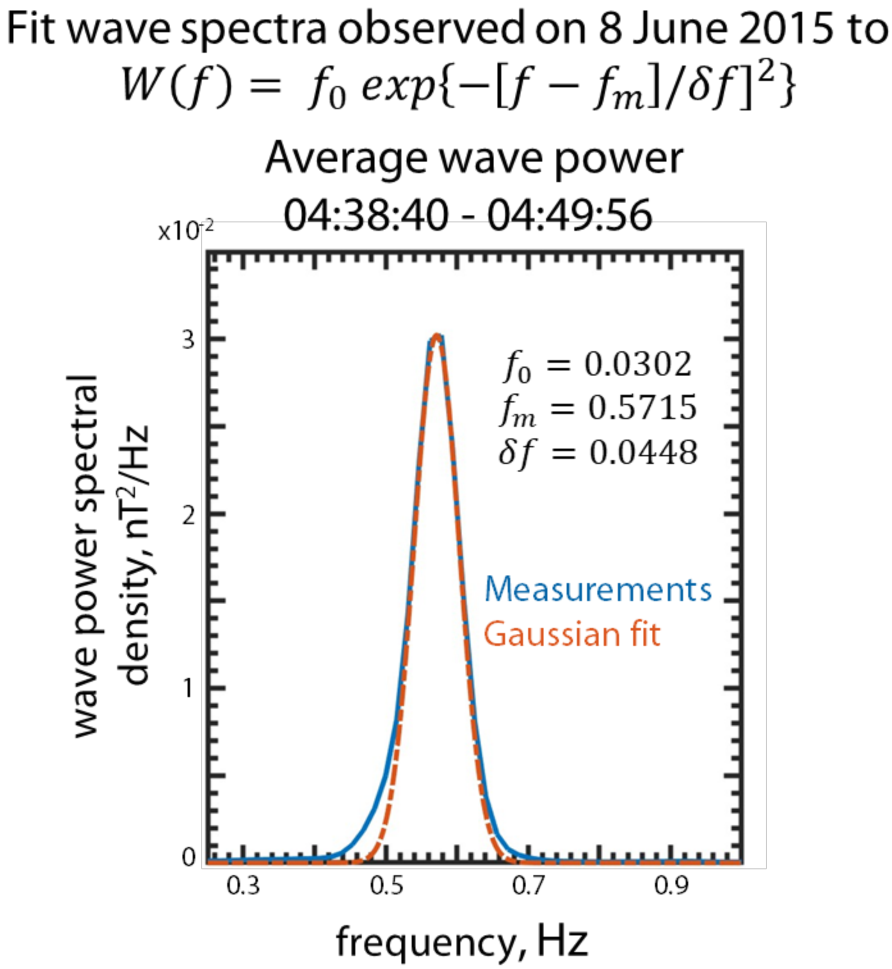

Figure 3 in the manuscript shows the wave power spectral density from 0 – 6 UT 8 June 2015. In Figure 3 we identified regions of EMIC power, including one region near 04:38:40 - 04:49:56 UT. Here, we time-average this wave power spectral density. This average power during this period is shown in blue in Figure S4. A Gaussian fit in red is prescribed to this peak, and matches the observations well.

Figure S5: Dispersion relationship results and resonant energy regions for representative He+ and O+ band EMIC waves

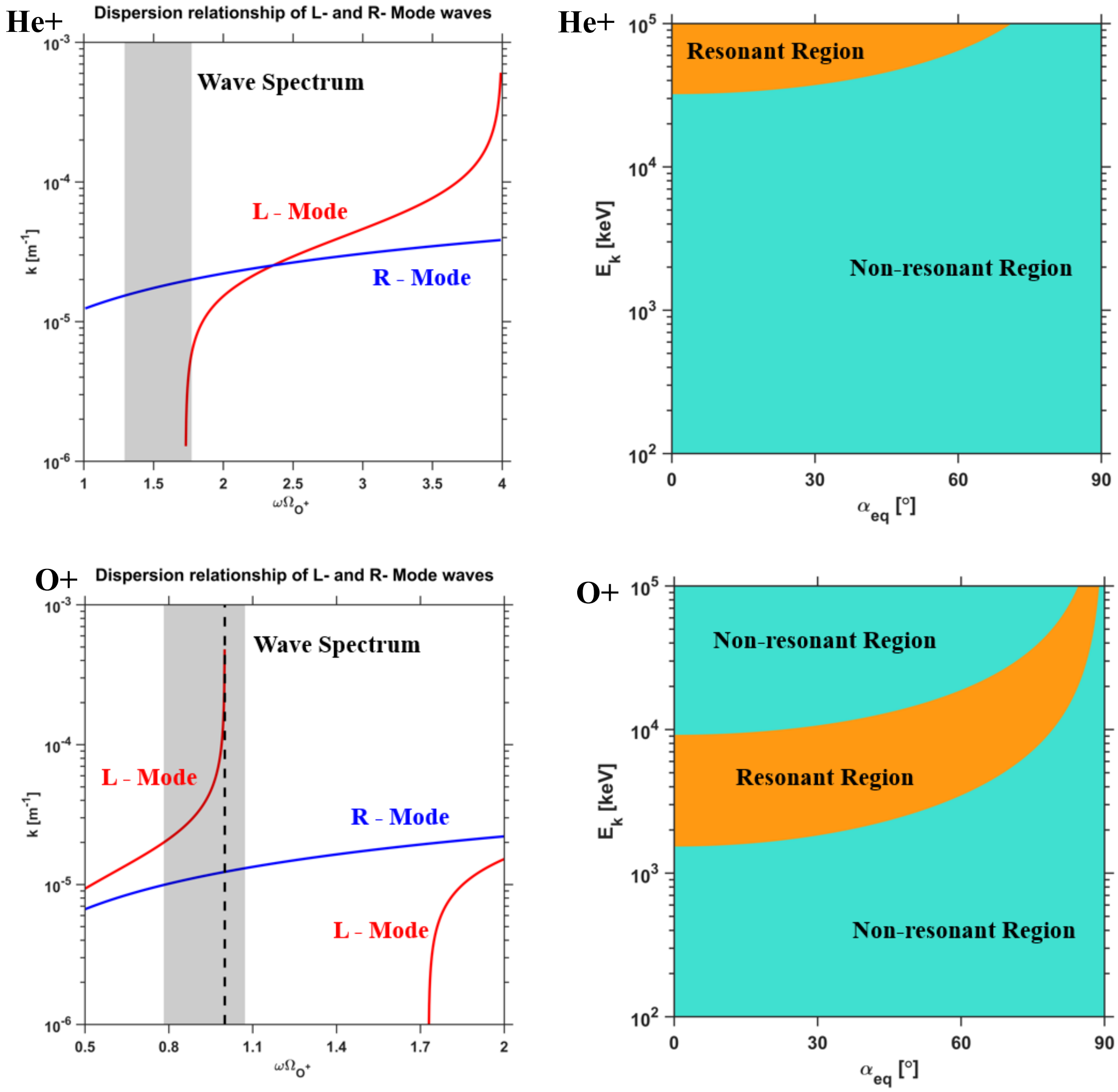

In this study we solve the cold plasma dispersion relation (e.g., Summer et al., 2007) by use of the Full Diffusion Code (Ni et al., 2008, 2011; Shprits and Ni et al., 2009). Here, we show results for the solution of the wave number k, as a function of frequency normalized to the oxygen gyrofrequency ω/Ω_{O+} for both cases considered in the paper. These two cases are, H+ band EMIC waves, and O+ band EMIC waves. The results of the dispersion relation are shown in the left panels for each of these two cases; The solution He+ band waves are shown in the top left panel, the solution for O+ band waves is shown in the bottom left panel. Both the L and R modes are shown here for completeness, while we consider only L-mode waves in this study due to their high occurrence rate from studies of EMIC waves during the Van Allen Probes era, discussed in the main text. The wave spectrum indicated on each plot is the width of the EMIC wave spectra observed just before the satellite crossing of L* = 3.5, in the He+ case this has been scaled according to the local magnetic field, in the O+ case, we maintain the frequency spectrum. Because this then shifts the spectra to frequencies greater than the O+ frequency, we then limit the actual wave spectra to 0.99 times the local O+ gyrofrequency.

On the right are the explicit resonant regions for each of the two wave types. Minimum resonant energies of electron with EMIC waves are discussed in the main text (see equation 2). For a full discussion of minimum resonant energies, we refer the reader to Summers et al., (2003). The resonant region for He+ band waves is shown in the top right, and shows minimum resonant energies of 32 MeV at 0 degree pitch angles and 56 MeV at 54 degree pitch angles (which corresponds to K = 0.10 $G^{1/2}R_E$) much higher than the energies of the observed loss feature discussed in this study. In the bottom right we show the explicit resonant region for O+ band EMIC waves, which here has minimum resonant energies of 1.4 MeV at 0 degree pitch angle, and 2.8 MeV at 54 degrees pitch angle. Thus, O+ band EMIC waves could be contributing to the loss of multi-MeV electrons, He+ band waves resonate here only with electron energies much higher than those observed to be lost during the event of study.

Figure S6: Energy and cross diffusion terms for both He+ and O+ band EMIC waves

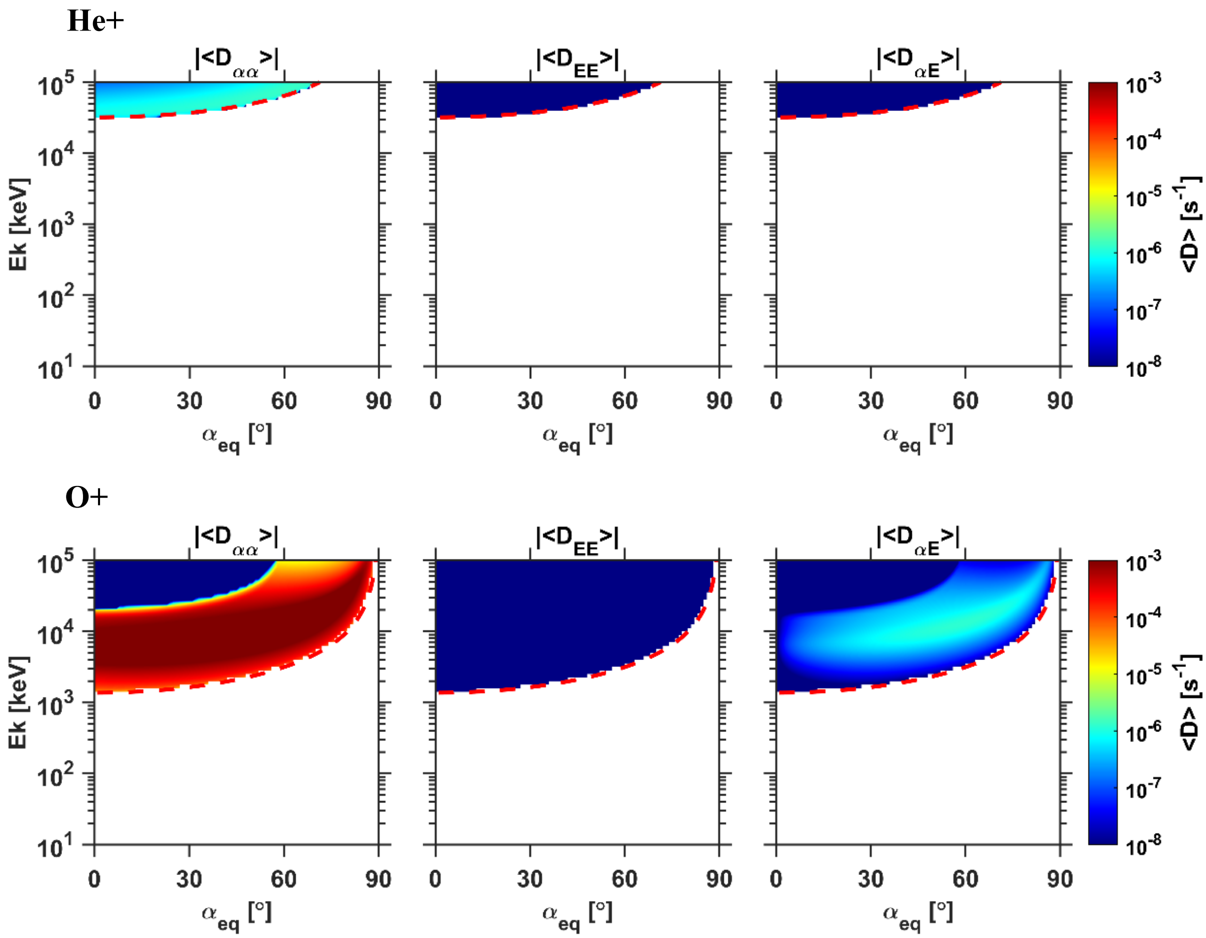

In this study we here consider only the effects of pitch angle scattering due to EMIC waves. EMIC waves can also cause energy diffusion and cross diffusion of trapped particles, the explicit equations for each of these diffusion coefficients is discussed in Summers et al., (2007). Here, we use the Full Diffusion Code (Ni et al., 2008, 2011; Shprits and Ni et al., 2009) to calculate these parameters. We compare the pitch angle diffusion coefficient $D_{\alpha\alpha}$ is with the energy diffusion coefficient D_{EE} and the cross diffusion coefficient $D_{\alpha\mathrm{E}}$ in Figure S6 for both He+ and O+ band EMIC wave cases discussed in the main text. When comparing the diffusion coefficients due to O+ band EMIC waves (bottom row), it is shown that D_{EE} is ~5 orders of magnitude less than $D_{\alpha\alpha}$ for the energies of interest, and $D_{\alpha\mathrm{E}}$ is about 3 orders of magnitude less than $D_{\alpha\alpha}$. Therefore, these other diffusion mechanisms are minor compared to the effects of pitch angle scattering here, and negligible. Thus, the pure-pitch angle diffusion model used here for PSD evolution is sufficient for modeling major effects of EMIC waves on the populations of study.

Figure S7: Observed and simulated PSD at μ = 1500, 2000, 2500, and 3000 MeV/G

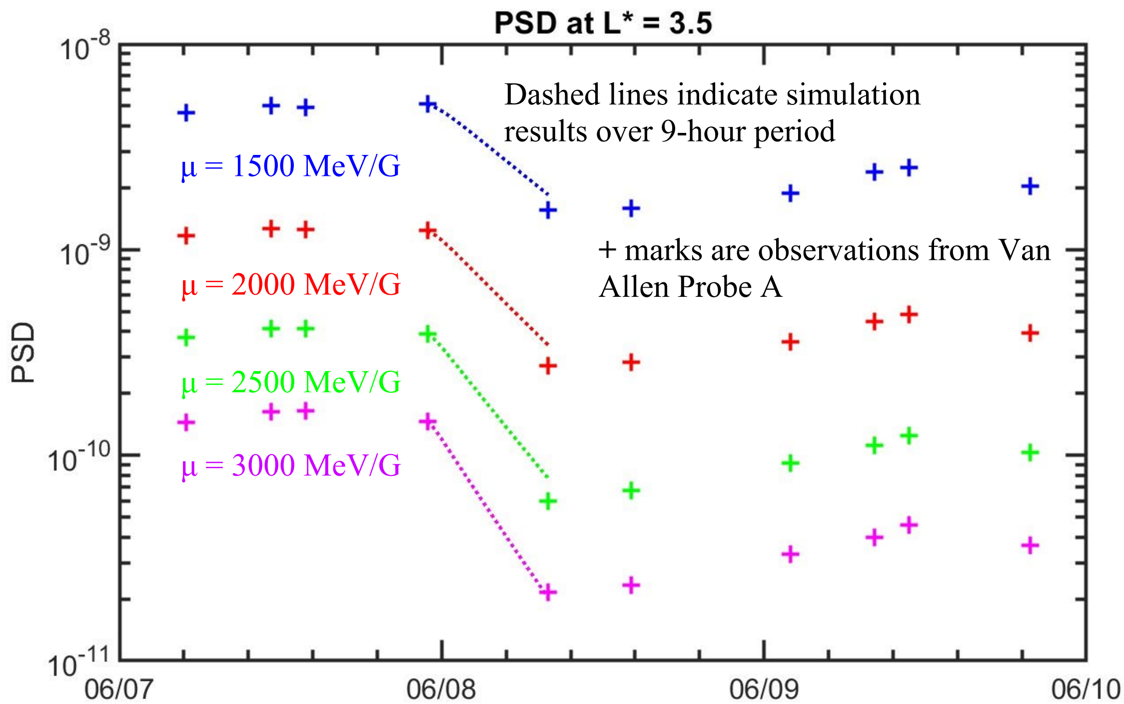

Figure 5 in the main text describes in detail the simulation result of PSD as a function of pitch angle for μ = 3000 MeV/G electrons, and compares the simulation results to observations from Van Allen Probe A. Here we show results for the complete set of diagnostic μ values discussed in this study, 1500, 2000, 2500, and 3000 MeV/G. These values correspond to 3.4, 4, 4.5, and 5.0 MeV electrons, respectively, at K = 0.10 $G^{1/2}R_E$, L* = 3.5, during the event of study when adiabatic coordinates are found with the TS04D magnetic field model. Here, marks indicated by "+" are observations from Van Allen Probe A at L* = 3.5, K = 0.10 $G^{1/2}R_E$ for the period 7 through 9 June 2015. Observations color coded to the μ labels on the plot.

PSD is simulated by prescribing initial PSD spectra and matching the PSD at 54° equatorial pitch angle to the observations (54° corresponds to K = 0.10 $G^{1/2}R_E$). The PSD is then simulated for 9 hours, the period during which rapid loss is observed here by Van Allen Probe A. The dashed lines represent the PSD simulation result, evaluated at 54°, over the 9 hour period simulated. These results show decrease from each energy comparable to the observations.

Figure S8: Partial ion composition and lack of oxygen torus presence

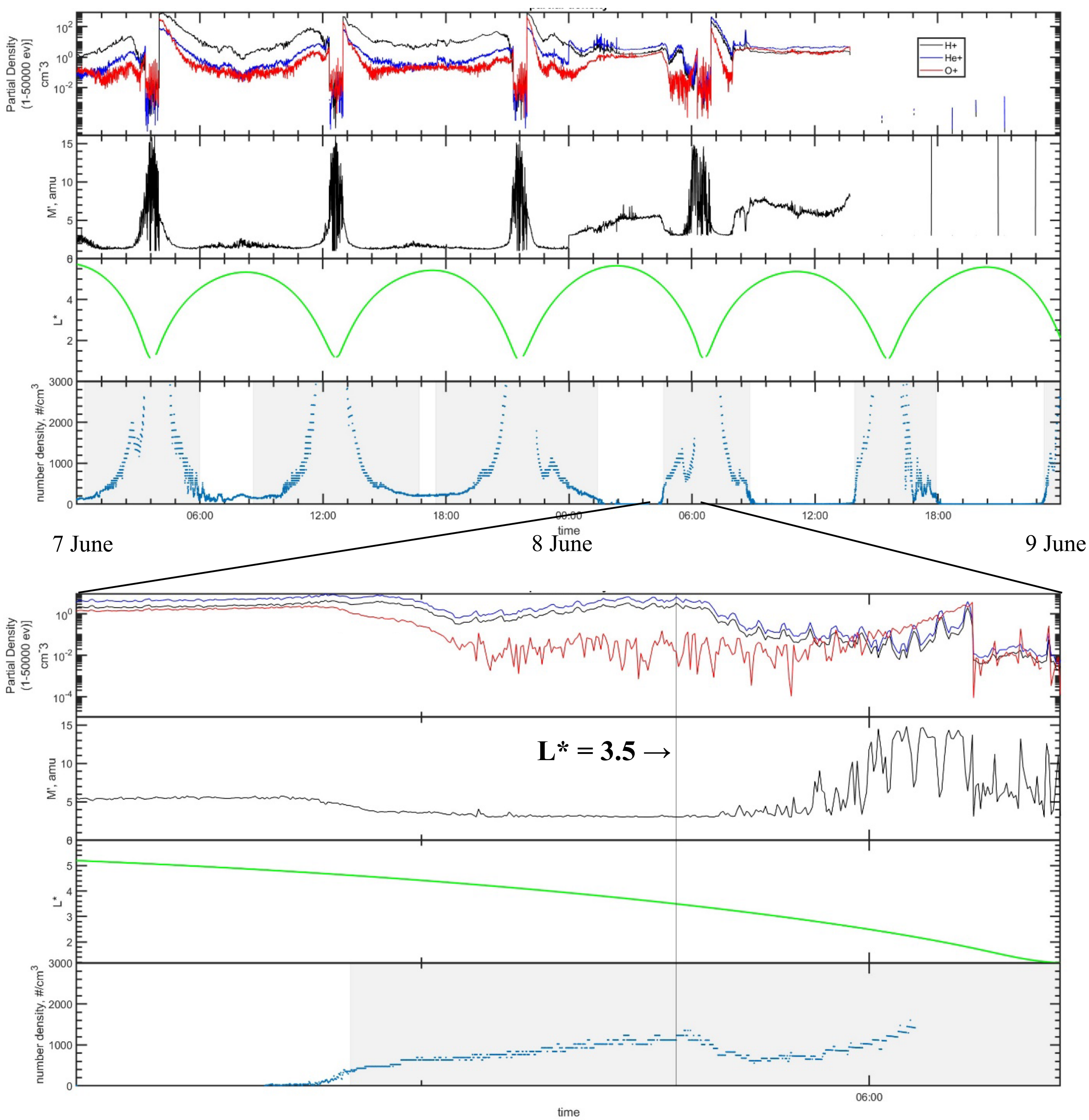

Studies by Yu et al., (2015) suggest that many O+ band EMIC waves are correlated with the oxygen torus (Nose et al., 2015), a region of dense oxygen that forms near the outer edge of the plasmasphere during certain periods. Nose et al., (2015) have studied HOPE data and used the methods of Goldstein et al., (2014) for calculating partial densities of ions for >eV energies (lower than the standard HOPE data product considers for ion densities). Nose et al., (2015) introduce the parameter M', the average mass density of the local plasma from the major species H+, He+, and O+, as found from this ion composition calculation from HOPE. Here, we calculate the partial ion densities and M' as described by Goldstein et al., (2014) and Nose et al., (2015) respectively, using data from Van Allen Probe A. The top panel of the first figure shown above is the partial ion composition. The second panel is M’. The third panel is the L* of the spacecraft corresponding to $K = 0.10\ G^{1/2}R_E$, and the fourth panel is the local number density as found from analysis of EMFISIS data. Shaded regions in the fourth panel indicate regions when the spacecraft is within the plasmapause, described prior. We show in the first figure this data for 7 through 9 June 2015 to show parameters before and after the event. HOPE data is unavailable for the second half of 8 June 2015.

In the lower figure, we show these same parameters, focused on the first inbound pass of the spacecraft on 8 June 2015 during which rapid PSD loss is observed. During this pass, there is no appreciable increase in M’, or the O+ partial ion composition near L* = 3.5. Rather, M’ does not increase until much lower, at L* < 3. Therefore, we do not find evidence of the oxygen torus at L* = 3.5 during this event.